IEEE Access
Multidisciplinary | Rapid Review | Open Access Journal

Received February 16, 2020, accepted February 24, 2020, date of publication March 4, 2020, date of current version March 12, 2020.

Digital Object Identifier 10.1109/ACCESS.2020.2977535

A Multivariate Optimal Control Strategy for the Attitude Tracking of a Parafoil-UAV System

FEIKAI LV, WEILIANG HE, AND LINGGONG ZHAO
School of Astronautics, Beihang University, Beijing 100191, China
Corresponding author: Weiliang He (heweiliang@buaa.edu.cn)

ABSTRACT The pendulum-swing problem is a factor that limits the development of parafoil-unmanned aerial vehicle (UAV) systems. Autonomous attitude control based on parafoil and UAV control mechanisms is considered an effective solution to this problem. However, due to the coupling effect of the two control mechanisms, conventional control methods are not suitable. The design of attitude control for parafoil-UAV systems has become a challenge. For this problem, a model-independent optimal control method called multivariate extremum seeking with the Newton method (ES-NM) is introduced in this paper. To assess the performance of multivariate ES-NM control for parafoil-UAV systems, a multibody dynamic model based on the flexible line assumption is built. The aerodynamic coefficients of this model are estimated via computational fluid dynamics (CFD) and corrected using flight data. Using this model, the coupling effect of the two control mechanisms is investigated, and the control range is determined. Finally, the effectiveness of multivariate ES-NM controller for a parafoil-UAV system is verified. Simulation experiments performed under various conditions demonstrate that the multivariate ES-NM control can manipulate the UAV control mechanism and the parafoil control mechanism simultaneously and produce the desired UAV attitude track. Additionally, comparisons to proportional-integral-derivative (PID) control reveal the better performance of the proposed control method.

INDEX TERMS Parafoil-UAV system, nonlinear multibody dynamic model, multivariate ES-NM control, attitude optimal control, attitude tracking.

I. INTRODUCTION

Parafoil systems are unique aerodynamic decelerator systems. Through asymmetric and symmetric deflections of the parafoil trailing edge, these decelerator systems can steer payloads to an intended point and perform flare maneuvers to ensure a soft landing. Hence, parafoil systems are well suited for fixed-wing unmanned aerial vehicles (UAV) that need to land on unprepared terrain accurately [1]. In recent years, this type of system has been used in several UAVs, including Developmental Sciences Corp.'s SkyEye, Israel Aerospace Industries' Eyeview and NASA's X-38 [2], [3]. However, the parafoil-UAV system has a unique issue called the pendulum-swing problem. This problem is caused by gusts and leads to instability in the attitude of the UAV [4]. If the pendulum angle is too large during landing, the weak structural parts of the UAV, such as the wings and tail, will impact the ground first and break apart.

A suitable method by which to solve the pendulum-swing problem involves designing a control strategy for the parafoil-UAV system. In recent studies, performing a flare maneuver against the wind has been demonstrated to be an effective approach to reduce the lateral and longitudinal velocities and prevent pendulum swinging of the system [5], [6]. Through in-flight wind identification, the wind direction and speed can be determined. The heading of a parafoil-UAV system is controlled by the asymmetric deflection of the parafoil trailing edge, and a guidance and control algorithm ensures that the heading is opposite to the wind direction. By coupling this strategy with a final flare maneuver, the UAV can achieve a soft and safe landing. However, in a variable-wind environment, this control strategy cannot completely stop the pendulum-swinging motion.

Another attractive control strategy is attitude control based on control mechanisms of the system, including

The associate editor coordinating the review of this manuscript and approving it for publication was Halil Ersin Soken.

asymmetric and symmetric deflections of the parafoil trailing edge and deflections of the aileron, elevator, and rudder of the UAV. During flight, the UAV in the parafoil-UAV system has a normal angle of attack. The UAV control mechanisms are effective and can steer the longitudinal and lateral motions. However, in recent years, few studies concerning the attitude control of the UAV in a parafoil-UAV system have been reported. The lack of a high-fidelity dynamic model and the complexity of the coupling effect caused by the parafoil and UAV control mechanisms make attitude control design challenging. In modeling, 8/9-degree-of-freedom (DoF) models for the parafoil-UAV system were presented first [7], [9], and a multibody dynamic model based on the flexible line assumption was then developed [10]. This multibody dynamic model can provide high accuracy and is suitable for assessing the control performance.

For other problems, an online optimal control method may be a good solution. Extremum seeking control (ESC) is a model-independent real-time optimal control approach for nonlinear dynamic problems [11]. By adjusting the plant input, this approach can converge the measured output to extrema. Many studies on ESC have been presented. The control performance of ESC was discussed in [12], and corresponding applications in engineering fields were presented in [13]–[15]. As mentioned in the references, this control method is generally used to solve single input-single output problems. For multi-input dynamic systems, this strategy needs to be further improved. Recently, Chun Yin proposed an improved method based on ESC, which is called multivariate extremum seeking with the Newton method (ES-NM) [16], [17]. This control method can solve multi-input problems, accelerate convergence without increasing oscillations and eliminate the coupling effect of multiple control mechanisms. It is suitable for addressing multi-input- single-output (MISO) control problems, such as the attitude control of parafoil-UAV systems. Hence, the purpose of this article is to design an attitude control strategy based on multivariate ES-NM to solve the pendulum-swing problem of parafoil-UAV systems.

To assess the performance of multivariate ES-NM control for parafoil-UAV systems, first, a multibody dynamic model based on the flexible line assumption is developed. All aerodynamic coefficients of this model are calculated by computational fluid dynamics (CFD) and are corrected by the flight data. The accuracy of the corrected model is reliable. Using this model, the coupling effect of the parafoil brake deflection and the UAV control mechanism can be ascertained. The control range of these two control mechanisms is then obtained. According to this range, the control parameters are determined, and the multivariate ES-NM controller is accomplished. Finally, a series of simulation experiments is performed under various conditions. The performance of multivariate ES-NM control for parafoil-UAV systems is explored and discussed.

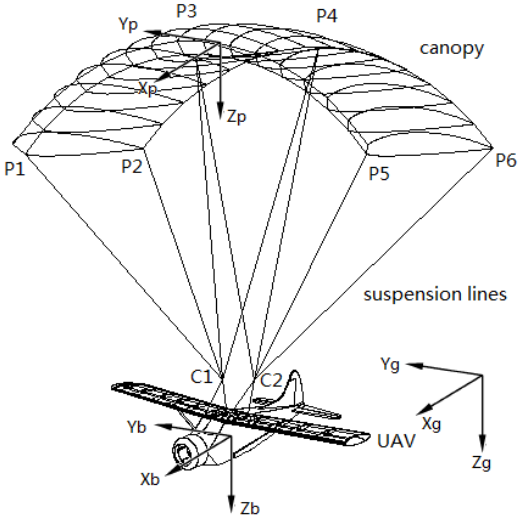

FIGURE 1. Configuration of the parafoil-UAV system.

II. PARAFOIL-UAV SYSTEM MODEL

There are three parts in a parafoil-UAV system: the parafoil, the UAV, and the suspension lines. As shown in Fig. 1, the connection between the parafoil and the UAV is a two-point rigging connection, which permits considerable relative yawing and pitching motions but little relative rolling motion between the parafoil and the UAV. According to this configuration, the parafoil-UAV system can be modeled in three parts. The coordinate system is listed in Table 1.

The first part of the model is the parafoil canopy. The modeling of the parafoil canopy has been studied for several years. Due to the air flowing into the canopy, an inflated shape can be maintained during flight. The parafoil canopy is always considered as a rigid body [18]–[20]. Thus, the parafoil canopy of a parafoil-UAV system can be modeled with 6 DoF. The force and moment acting upon the parafoil canopy have contributions from the weight, the aerodynamic force and moment, the suspension line tension, and the apparent mass force and moment. By summing the forces and moments about the canopy mass center in the parafoil body reference frame, the dynamic equations of motion can be written as

$$m_p\dot{\boldsymbol{V}}_p+\boldsymbol{W}_p\times m_p\boldsymbol{V}_p=\boldsymbol{F}_{aerop}+\boldsymbol{G}_p+\boldsymbol{F}_{am}+\sum_{i=1}^{n}\boldsymbol{L}_{pg}\boldsymbol{T}_{p,i} \tag{1}$$

$$\boldsymbol{J}_p\dot{\boldsymbol{W}}_p+\mathbf{W}_p\times\left(\boldsymbol{J}_p\mathbf{W}_p\right)=\boldsymbol{M}_{aerop}+\boldsymbol{M}_{ai}+\sum_{i=1}^{n}\boldsymbol{l}_{p,i}\times\left(\boldsymbol{L}_{pg}\boldsymbol{T}_{p,i}\right) \tag{2}$$

In (1) and (2), m_p and $\boldsymbol{J}_p$ are the mass and inertia matrix of the parafoil canopy, respectively; $\boldsymbol{V}_p$ and $\boldsymbol{W}_p$ are the velocity and angular velocity of the parafoil canopy in the parafoil body reference frame; $\boldsymbol{F}_{aerop}$ and $\boldsymbol{M}_{aerop}$ are the parafoil aerodynamic force and moment; $\boldsymbol{F}_{am}$ and $\boldsymbol{M}_{ai}$ are the apparent mass force and inertia moment; $\boldsymbol{G}_p$ is the gravity of the

TABLE 1. Coordinate system.

Name	Definition
Inertial reference frame	Origin: arbitrary point at sea level; X_g axis: pointing north; Y_g axis: pointing east; Z_g axis: pointing down.
Parafoil body reference frame	Origin: parafoil mass center; X_p axis: pointing forward parallel to the parafoil chord; Y_p axis: pointing to right perpendicular to the symmetry plane of the parafoil; Z_p axis: pointing down perpendicular to the X_p-Y_p plane.
UAV body reference frame	Origin: UAV mass center; X_b axis: pointing toward the UAV nose; Y_b axis: pointing to the right, perpendicular to the symmetry plane of the UAV; Z_b axis: pointing down, perpendicular to the X_b-Y_b plane.
Parafoil aerodynamic reference frame	Origin: parafoil aerodynamic center; X_{ap} axis: pointing in the direction of the parafoil velocity vector relative to the air; Y_{ap} axis: pointing to the right, perpendicular to the X_{ap}-Z_{ap} plane; Z_{ap} axis: pointing down, perpendicular to the X_{ap} axis in the symmetry plane of the parafoil.
UAV aerodynamic reference frame	Origin: UAV aerodynamic center; X_{ab} axis: pointing in the direction of the UAV velocity vector relative to the air; Y_{ab} axis: pointing to the right, perpendicular to the X_{ab}-Z_{ab} plane; Z_{ab} axis: pointing down, perpendicular to the X_{ab} axis in the symmetry plane of the UAV.
Line reference frame	Origin: midway between points C1 and C2; X_l axis, Y_l axis, and Z_l axis: parallel to the X_g axis, Y_g axis, and Z_g axis, respectively.

parafoil canopy in the parafoil body reference frame; n is the number of suspension lines; the vector $\boldsymbol{T}_{p,i}$ represents the force of each suspension line; the vector $\boldsymbol{l}_{p,i}$ represents the position vector from the mass center of the parafoil canopy to the connection points P1, P2, P3. . .; and the matrix $\boldsymbol{L}_{pg}$ represents the transformation matrix from the inertial reference frame to the parafoil body reference frame.

The roll, pitch and yaw Euler angles of the parafoil canopy are represented by ϕ_p, θ_p, and ψ_p. The kinematic equations of the parafoil canopy are expressed as

$$\begin{bmatrix} \dot{\phi}_p \\ \dot{\theta}_p \\ \dot{\psi}_p \end{bmatrix} = \begin{bmatrix} 1 & \sin\phi_p \tan\theta_p & \cos\phi_p \tan\theta_p \\ 0 & \cos\phi_p & -\sin\phi_p \\ 0 & \sin\phi_p/\cos\theta_p & \cos\phi_p/\cos\theta_p \end{bmatrix} \begin{bmatrix} p_p \\ q_p \\ r_p \end{bmatrix} \tag{3}$$

where p_p, q_p, and r_p are the angular velocity components of the parafoil canopy in the parafoil body reference frame.

The parafoil aerodynamic forces $\boldsymbol{F}_{aerop}$ and moments $\boldsymbol{M}_{aerop}$ expressed in the parafoil body reference frame are provided in (4) and (5).

$$\boldsymbol{F}_{aerop} = \frac{1}{2}\rho \tilde{V}_p^2 S_p \boldsymbol{L}_{AP} \begin{bmatrix} -C_D^p \\ C_{y\beta}\beta_p \\ -C_L^p \end{bmatrix} \tag{4}$$

$$\boldsymbol{M}_{aerop} = \frac{1}{2}\rho \tilde{V}_p^2 S_p \begin{bmatrix} bC_l^p \\ cC_m^p \\ bC_n^p \end{bmatrix} \tag{5}$$

where ρ is the air density; b is the canopy span; c is the canopy chord; S_p is the reference area of the parafoil canopy; $\tilde{V}_p$ is the total velocity of the parafoil canopy; and the matrix $\boldsymbol{L}_{AP}$ represents the transformation matrix from the parafoil aerodynamic reference frame to the parafoil body reference frame.

The aerodynamic coefficients appearing in (4) and (5) depend on the angle of attack α_p, the sideslip angle β_p and the parafoil control inputs (asymmetric parafoil brake deflection δ_a^p and symmetric parafoil brake deflection δ_s^p) [21]. The static and dynamic stability derivatives and control derivatives can be calculated via CFD.

$$C_L^p = C_{L0} + C_{L\alpha}\alpha_p + C_{L\delta s}\delta_s^p \tag{6}$$

$$C_D^p = C_{D0} + C_{D\alpha^2}\alpha_p^2 + C_{D\delta s}\delta_s^p \tag{7}$$

$$C_l^p = C_{l\beta}\beta_p + \frac{b}{2\tilde{V}_p}C_{lp}p_p + \frac{b}{2\tilde{V}_p}C_{lr}r_p + C_{l\delta a}\delta_a^p \tag{8}$$

$$C_m^p = C_{m0} + C_{m\alpha}\alpha_p + \frac{c}{2\tilde{V}_p}C_{mq}q_p \tag{9}$$

$$C_n^p = C_{n\beta}\beta_p + \frac{b}{2\tilde{V}_p}C_{np}p_p + \frac{b}{2\tilde{V}_p}C_{nr}r_p + C_{n\delta a}\delta_a^p \tag{10}$$

The apparent mass force $\boldsymbol{F}_{am}$ and apparent inertia moment $\boldsymbol{M}_{ai}$ in the parafoil dynamic equations cannot be neglected because of the small mass-to-volume ratio of the parafoil canopy. The influences of the apparent mass and the apparent inertia have been demonstrated, and the methods by which to determine these apparent parameters are presented by Lissman and Barrows [22], [23]. According to the method of Lissman, the spanwise camber of the parafoil canopy can be neglected. The apparent mass forces and moments are expressed as

$$\boldsymbol{F}_{am} = -\boldsymbol{I}_{am}\dot{\tilde{\boldsymbol{V}}}_a - \boldsymbol{W}_p \times \boldsymbol{I}_{am}\left(\tilde{\boldsymbol{V}}_a\right) \tag{11}$$

$$\boldsymbol{M}_{ai} = -\left(\boldsymbol{I}_{ai}\dot{\boldsymbol{W}}_p + \boldsymbol{W}_p \times \left(\boldsymbol{I}_{ai}\boldsymbol{W}_p\right)\right) + \boldsymbol{r}_{am} \times \boldsymbol{F}_{am} \tag{12}$$

$$\tilde{\boldsymbol{V}}_a = \boldsymbol{V}_p - \boldsymbol{r}_{am} \times \boldsymbol{W}_p - \boldsymbol{L}_{pg}\boldsymbol{V}_{wind} \tag{13}$$

$$\dot{\tilde{\boldsymbol{V}}}_a = \dot{\boldsymbol{V}}_p - \boldsymbol{r}_{am} \times \dot{\boldsymbol{W}}_p - \boldsymbol{L}_{pg}\dot{\boldsymbol{V}}_{wind} + \boldsymbol{W}_p \times \boldsymbol{L}_{pg}\boldsymbol{V}_{wind} \tag{14}$$

where $\tilde{\boldsymbol{V}}_a$ is the airspeed vector of the apparent mass center in the body reference frame; $\boldsymbol{V}_{wind}$ is the wind velocity vector in the inertial reference frame; $\boldsymbol{r}_{am}$ is the position vector from the parafoil canopy mass center to the apparent mass center; and the matrices $\boldsymbol{I}_{am}$ and $\boldsymbol{I}_{ai}$ are the apparent mass and inertia matrixes of the parafoil canopy, which are discussed in [22].

The second part of the model is the UAV. The equations of motion for the UAV are derived with the Newton method [24], [25]. The UAV contends with gravity, aerodynamic forces and the tension of the suspension lines. By summing all forces and moments, the dynamic equations of the UAV in the UAV body reference frame can be written as

$$m_b\dot{\boldsymbol{V}}_b + \boldsymbol{W}_b \times m_b\boldsymbol{V}_b = \boldsymbol{G_b} + \boldsymbol{F_{aerob}} + \sum_{i=1}^{m}\boldsymbol{L}_{bg}\boldsymbol{T}_{b,i} \tag{15}$$

$$\boldsymbol{J}_b\dot{\boldsymbol{W}}_b+\boldsymbol{W}_b\times(\boldsymbol{J}_b\boldsymbol{W}_b)=\boldsymbol{M}_{\boldsymbol{aerob}}+\sum_{i=1}^{m}\boldsymbol{l}_{\boldsymbol{b},\boldsymbol{i}}\times\left(\boldsymbol{L}_{bg}\boldsymbol{T}_{b,\boldsymbol{i}}\right) \quad (16)$$

In (15) and (16), m_b and $\boldsymbol{J}_b$ are the mass and inertia matrix of the UAV, respectively; $\boldsymbol{V}_b$ and $\boldsymbol{W}_b$ are the velocity and angular velocity of the UAV mass center in the UAV body reference frame; $\boldsymbol{G}_b$ is the gravity of the UAV; the vector $\boldsymbol{T}_{b,i}$ represents the force of the suspension line attached to the UAV; the vector $\boldsymbol{l}_{p,i}$ is the position vector from the UAV mass center to the connection points B1, B2, B3, B4. . .; and the matrix $\boldsymbol{L}_{bg}$ represents the transformation matrix from the inertial reference frame to the UAV body reference frame.

The kinematic equations of the UAV can be written as

$$\begin{bmatrix}\dot{\phi}_b\\ \dot{\theta}_b\\ \dot{\psi}_b\end{bmatrix}=\begin{bmatrix}1 & \sin\phi_b\tan\theta_b & \cos\phi_b\tan\theta_b\\ 0 & \cos\phi_b & -\sin\phi_b\\ 0 & \sin\phi_b/\cos\theta_b & \cos\phi_b/\cos\theta_b\end{bmatrix}\begin{bmatrix}p_b\\ q_b\\ r_b\end{bmatrix} \quad (17)$$

where ϕ_b, θ_b, and ψ_b are the roll, pitch and yaw Euler angles of the UAV, respectively, and p_p, q_p, and r_p are the angular velocity components of the UAV in the UAV body reference frame.

The UAV aerodynamic forces $\boldsymbol{F}_{aerob}$ and moments $\boldsymbol{M}_{aerob}$ can be written as

$$\boldsymbol{F}_{aerob}=\frac{1}{2}\rho\tilde{V}_b^2S_b\boldsymbol{L}_{ab}\begin{bmatrix}-C_D^b\\ C_Y^b\\ -C_L^b\end{bmatrix} \quad (18)$$

$$\boldsymbol{M}_{aerob}=\frac{1}{2}\rho\tilde{V}_b^2S_b\begin{bmatrix}b_bC_l^b\\ c_bC_m^b\\ b_bC_n^b\end{bmatrix} \quad (19)$$

where $\tilde{V}_b$ is the airspeed of the UAV; b_b is the UAV wing span; c_b is the UAV wing chord; S_b is the reference area of the UAV; and the matrix $\boldsymbol{L}_{ab}$ represents the transformation matrix from the UAV aerodynamic reference frame to the UAV body reference frame.

The UAV aerodynamic coefficients are functions of the angle of attack α_b, the sideslip angle β_b and the UAV control inputs (aileron angle δ_a^b, elevator angle δ_e^b, and rudder angle δ_r^b). The functions can be written as

$$C_D^b=C_{D0}^b+\frac{\left(C_L^b-C_{L0}^b\right)^2}{\pi eAR}+C_{D\delta e}^b\delta_e^b+C_{D\delta a}^b\delta_a^b+C_{D\delta r}^b\delta_r^b \quad (20)$$

$$C_Y^b=C_{y\beta}^b\beta_b+C_{y\delta a}^b\delta_a^b+C_{y\delta r}^b\delta_r^b+\frac{b_b}{2\tilde{V}_b}\left(C_{yp}^bp_b+C_{yr}^br_b\right) \quad (21)$$

$$C_L^b=C_{L0}^b+C_{L\alpha}^b\alpha_b+C_{L\delta e}^b\delta_e^b+\frac{c_b}{2\tilde{V}_b}\left(C_{L\dot{\alpha}}^b\dot{\alpha}_b+C_{Lq}^bq_b\right) \quad (22)$$

$$C_l^b=C_{l\beta}^b\beta_b+\frac{b_b}{2\tilde{V}_b}C_{lp}^bp_b+\frac{b_b}{2\tilde{V}_b}C_{lr}^br_b+C_{l\delta a}^b\delta_a^b+C_{l\delta r}^b\delta_r^b \quad (23)$$

$$C_m^b=C_{m0}^b+C_{m\alpha}^b\alpha_b+C_{m\delta e}^b\delta_e^b+\frac{c_b}{2\tilde{V}_b}\left(C_{m\dot{\alpha}}^b\dot{\alpha}_b+C_{mq}^bq_b\right) \quad (24)$$

$$C_n^b=C_{n\beta}^b\beta_b+\frac{b_b}{2\tilde{V}_b}C_{np}^bp_b+\frac{b_b}{2\tilde{V}_b}C_{nr}^br_b+C_{n\delta a}^b\delta_a^b+C_{n\delta r}^b\delta_r^b \quad (25)$$

where e is the Oswald coefficient and AR is the aspect ratio of the UAV wing. The UAV stability and control derivatives appearing in (20)-(25) are constant. All of these derivatives can also be estimated via CFD.

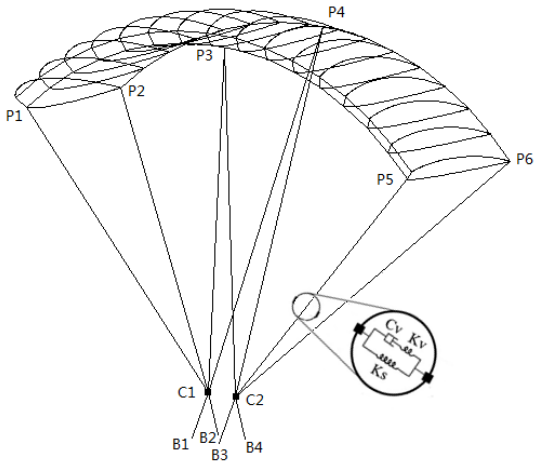

FIGURE 2. Suspension line schematic.

The last part of the model is the suspension lines. According to the configuration of the parafoil-UAV system, as shown in Fig. 2, all of the suspension lines are simplified as 12 standard massless viscoelastic elements, of which eight elements are attached to the parafoil and four elements are attached to the UAV. This viscoelastic element has been applied to the modeling of the flexible line, such as the tether of the towed parafoil system and the rope of the dragline excavation system [26], [27]. Consider two mass points C1 and C2, with the masses of all the suspension lines symmetrically focused on these two mass points. The forces on the two points include the weight, aerodynamic forces and tension of the suspension lines. By summing all of these forces, the dynamic equations of the suspension line in the line reference frame are expressed as

$$m_{c1}\dot{\boldsymbol{V}}_{c1}=\sum_{i=1}^{n_{c1}}\boldsymbol{F}_{\boldsymbol{p},c1,\boldsymbol{i}}+\sum_{i=1}^{m_{c1}}\boldsymbol{F}_{\boldsymbol{b},c1,\boldsymbol{i}}+\boldsymbol{F}_{aero,c1}+\boldsymbol{G}_{c1} \quad (26)$$

$$m_{c2}\dot{\boldsymbol{V}}_{c2}=\sum_{i=1}^{n_{c2}}\boldsymbol{F}_{\boldsymbol{p},c2,\boldsymbol{i}}+\sum_{i=1}^{m_{c2}}\boldsymbol{F}_{\boldsymbol{b},c2,\boldsymbol{i}}+\boldsymbol{F}_{aero,c2}+\boldsymbol{G}_{c2} \quad (27)$$

In (26) and (27), m_{c1} and m_{c2} are the total masses of suspension lines attached to points C1 and C2; $\boldsymbol{V}_{c1}$ and $\boldsymbol{V}_{c2}$ are the velocity vectors of the mass points C1 and C2 in the line reference frame, respectively; $\boldsymbol{G}_{c1}$ and $\boldsymbol{G}_{c2}$ are the gravity of mass points;n_{c1} and n_{c2} are the number of suspension lines that connect the parafoil canopy to points C1 and C2; m_{c1} and m_{c2} are the number of suspension lines that connect the UAV to points C1 and C2; and $\boldsymbol{F}_{aero,c1}$ and $\boldsymbol{F}_{aero,c2}$ are the aerodynamic forces on the suspension lines, which can be neglected for a small parafoil.

The forces of the suspension lines, $\boldsymbol{F}_{p,c1,i}$, $\boldsymbol{F}_{p,c2,i}$, $\boldsymbol{F}_{b,c1,i}$, and $\boldsymbol{F}_{b,c2,i}$, are expressed in terms of the strain and strain rate of the suspension lines. The corresponding expressions can

be written as

$$\boldsymbol{F}_{p,c1,i}, \boldsymbol{F}_{p,c2,i}, \boldsymbol{F}_{b,c1,i} \text{ or } \boldsymbol{F}_{b,c2,i} = \frac{F_{Ti}}{l_{Ti}} \begin{bmatrix} \Delta x_i \\ \Delta y_i \\ \Delta z_i \end{bmatrix} \tag{28}$$

$$\dot{F}_{Ti} + \frac{K_v}{C_v} F_{Ti} = \begin{cases} (K_s + K_v)\, \dot{l}_{Ti} + \dfrac{K_v K_s}{C_v} (l_{Ti} - l) & (l_{Ti} > l) \\ 0 \quad (l_{Ti} \le l) \end{cases} \tag{29}$$

$$l_{Ti} = \sqrt{\Delta x_i^2 + \Delta y_i^2 + \Delta z_i^2} \tag{30}$$

where F_{Ti} is the tension of each suspension line element; Δx_i, Δy_i, and Δz_i are the position difference components; l_{Ti} and $\dot{l}_{Ti}$ are the length and strain rate of each suspension line; l is the nominal unstretched line length; and K_s, K_v and C_v are the static stiffness, viscous stiffness and viscous damping coefficients of a viscoelastic line element, respectively. For a flexible suspension line, if $l_{Ti} \le l$, the tension of the line element will be equal to zero.

For the same suspension line, the tension acting upon the parafoil canopy or the UAV is equal to the tension acting upon the two mass points. The directions of these two force vectors are opposite. Hence, the vectors $\boldsymbol{T}_{p,i}$ and $\boldsymbol{T}_{b,i}$ can be expressed as

$$\sum_{i=1}^{n} \boldsymbol{T}_{p,i} = -\sum_{i=1}^{n_{c1}} \boldsymbol{F}_{p,c1,i} - \sum_{i=1}^{n_{c2}} \boldsymbol{F}_{p,c2,i}, \quad n = n_{c1} + n_{c2} \tag{31}$$

$$\sum_{i=1}^{m} \boldsymbol{T}_{b,i} = -\sum_{i=1}^{m_{c1}} \boldsymbol{F}_{b,c1,i} - \sum_{i=1}^{m_{c2}} \boldsymbol{F}_{b,c2,i}, \quad m = m_{c1} + m_{c2} \tag{32}$$

Finally, the dynamic equations of the parafoil-UAV system are formed by combining (1), (2), (15), (16), (26), and (27). The set of 6 translational and rotational dynamic equations yields 18 scalar equations of motion that can be written in matrix form. The matrix equations for the parafoil-UAV system are expressed as (33), as shown at the bottom of this page, where $\boldsymbol{S}(\cdot)$ is the cross-product matrix of the vector and B_1, B_2, B_3, B_4, B_5, and B_6 are written as

$$\begin{aligned} B_1 = {} & \boldsymbol{F}_{aerop} + \boldsymbol{G}_p - \sum_{i=1}^{n_{c1}} \boldsymbol{L}_{pg} \boldsymbol{F}_{p,c1,i} - \sum_{i=1}^{n_{c2}} \boldsymbol{L}_{pg} \boldsymbol{F}_{p,c2,i} \\ & - \boldsymbol{S}\left(\boldsymbol{W}_p\right) \boldsymbol{I}_{am} \left(\boldsymbol{V}_p - \boldsymbol{S}\left(\boldsymbol{r}_{am}\right) \boldsymbol{W}_p - \boldsymbol{L}_{pg} \boldsymbol{V}_{wind}\right) \\ & + \boldsymbol{I}_{am} \boldsymbol{L}_{pg} \dot{\boldsymbol{V}}_{wind} \\ & - \boldsymbol{I}_{am} \boldsymbol{S}\left(\boldsymbol{W}_p\right) \boldsymbol{L}_{pg} \boldsymbol{V}_{wind} - \boldsymbol{S}\left(\boldsymbol{W}_p\right) m_p \boldsymbol{V}_p \end{aligned} \tag{34}$$

$$\begin{aligned} B_2 = {} & \boldsymbol{M}_{aerop} - \boldsymbol{S}\left(\boldsymbol{W}_p\right) \boldsymbol{J}_p \boldsymbol{W}_p - \sum_{i=1}^{n_{c1}} \boldsymbol{l}_{p,c1,i} \times \left(\boldsymbol{L}_{pg} \boldsymbol{F}_{p,c1,i}\right) \\ & - \sum_{i=1}^{n_{c2}} \boldsymbol{l}_{p,c2,i} \times \left(\boldsymbol{L}_{pg} \boldsymbol{F}_{p,c2,i}\right) - \boldsymbol{S}\left(\boldsymbol{W}_p\right) \boldsymbol{I}_{ai} \boldsymbol{W}_p \\ & + \boldsymbol{S}\left(\boldsymbol{r}_{am}\right) \boldsymbol{I}_{am} \left(\boldsymbol{L}_{pg} \dot{\boldsymbol{V}}_{wind} - \boldsymbol{S}\left(\boldsymbol{W}_p\right) \boldsymbol{L}_{pg} \boldsymbol{V}_{wind}\right) \\ & - \boldsymbol{S}\left(\boldsymbol{r}_{am}\right) \boldsymbol{S}\left(\boldsymbol{W}_p\right) \boldsymbol{I}_{am} \left(\boldsymbol{V}_p - \boldsymbol{S}\left(\boldsymbol{r}_{am}\right) \boldsymbol{W}_p - \boldsymbol{L}_{pg} \boldsymbol{V}_{wind}\right) \end{aligned} \tag{35}$$

$$\begin{aligned} B_3 = {} & \boldsymbol{G}_{\boldsymbol{b}} + \boldsymbol{F}_{\boldsymbol{aerob}} - \sum_{i=1}^{m_{c1}} \boldsymbol{L}_{bg} \boldsymbol{F}_{b,c1,\boldsymbol{i}} - \sum_{i=1}^{m_{c2}} \boldsymbol{L}_{bg} \boldsymbol{F}_{b,c2,\boldsymbol{i}} \\ & - S\left(\boldsymbol{W}_b\right) m_b \boldsymbol{V}_b \end{aligned} \tag{36}$$

$$\begin{aligned} B_4 = {} & \boldsymbol{M}_{\boldsymbol{aerob}} - \boldsymbol{S}\left(\boldsymbol{W}_b\right) \boldsymbol{J}_b \boldsymbol{W}_b \\ & - \sum_{i=1}^{m_{c1}} \boldsymbol{l}_{\boldsymbol{b},c1,\boldsymbol{i}} \times \left(\boldsymbol{L}_{bg} \boldsymbol{F}_{b,c1,\boldsymbol{i}}\right) - \sum_{i=1}^{m_{c2}} \boldsymbol{l}_{\boldsymbol{b},c2,i} \times \left(\boldsymbol{L}_{bg} \boldsymbol{F}_{b,c2,\boldsymbol{i}}\right) \end{aligned} \tag{37}$$

$$B_5 = \sum_{i=1}^{n_{c1}} \boldsymbol{F}_{\boldsymbol{p},c1,\boldsymbol{i}} + \sum_{i=1}^{m_{c1}} \boldsymbol{F}_{\boldsymbol{b},c1,\boldsymbol{i}} + \boldsymbol{F}_{aero,c1} + \boldsymbol{G}_{c1} \tag{38}$$

$$B_6 = \sum_{i=1}^{n_{c2}} \boldsymbol{F}_{\boldsymbol{p},c2,\boldsymbol{i}} + \sum_{i=1}^{m_{c2}} \boldsymbol{F}_{\boldsymbol{b},c2,\boldsymbol{i}} + \boldsymbol{F}_{aero,c2} + \boldsymbol{G}_{c2} \tag{39}$$

III. MULTIVARIATE EXTREMUM SEEKING CONTROL

Consider a state vector x and an output vector y. The model of the prafoil-UAV system are then written as

$$\dot{x} = f(x, u) = F(x) + G(x)\, u, \quad y = g(x) \tag{40}$$

where F, G, f and g are smooth nonlinear functions; and u is the control input.

Suppose that we know a smooth control law $u = \varphi(\vartheta)$ parametrized by ϑ. The model of the parafoil-UAV system can then be expressed as $\dot{x} = f(x, \varphi(\vartheta))$. There exists a smooth function χ such that $f(x, \varphi(\vartheta)) = 0$ if and only if $x = \chi(\vartheta)$. Additionally, for every $\vartheta \in R^n$, the equilibrium $x = \chi(\vartheta)$ of the system $\dot{x} = f(x, \varphi(\vartheta))$ is locally exponentially stable.

The quadratic cost function of this system is written as

$$z = h(y) = (\tilde{w} - y)^T \boldsymbol{E} (\tilde{w} - y) = h(g(x)) \tag{41}$$

$$\begin{bmatrix} m_p \boldsymbol{I} + \boldsymbol{I}_{am} & -\boldsymbol{I}_{am} \boldsymbol{S}\left(\boldsymbol{r}_{am}\right) & & & & \\ \boldsymbol{S}\left(\boldsymbol{r}_{am}\right) \boldsymbol{I} & \boldsymbol{J}_p + \boldsymbol{I}_{ai} - \boldsymbol{S}\left(\boldsymbol{r}_{am}\right) \boldsymbol{I}_{am} \boldsymbol{S}\left(\boldsymbol{r}_{am}\right) & & & & \\ & & m_b \boldsymbol{I} & & & \\ & & & \boldsymbol{J}_b & & \\ & & & & m_{c1} \boldsymbol{I} & \\ & & & & & m_{c2} \boldsymbol{I} \end{bmatrix} \begin{bmatrix} \dot{V}_p \\ \dot{W}_p \\ \dot{V}_b \\ \dot{W}_b \\ \dot{V}_{c1} \\ \dot{V}_{c2} \end{bmatrix} = \begin{bmatrix} B_1 \\ B_2 \\ B_3 \\ B_4 \\ B_5 \\ B_6 \end{bmatrix} \tag{33}$$

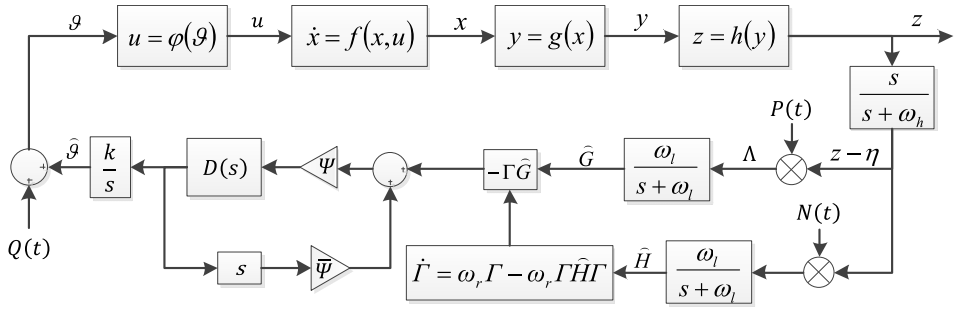

FIGURE 3. Block diagram of the multivariate ES-NM for a parafoil-UAV system.

where $\tilde{w}$ is the desired attitude. In this cost function, there exists a unique $\vartheta^* \in R^n$ for $z = h(g(\chi(\vartheta))) = \tilde{h}(\vartheta)$ such that $\frac{\partial}{\partial\vartheta}\tilde{h}(\vartheta^*) = 0$ and $\frac{\partial^2}{\partial\vartheta^2}\tilde{h}(\vartheta^*) = H > 0, H = H^T$. The attitude control problem of the parafoil-UAV system is transformed into an extremum seeking problem of the cost function.

To search the minimum $z = \tilde{h}(\vartheta)$ at ϑ^*, a multivariate extremum seeking with the Newton method is proposed in this paper. The scheme of multivariate ES-NM is presented in Fig.3, and the functions are expressed as

$$\frac{dx}{dt} = f\left(x, \varphi\left(\hat{\vartheta} + Q(t)\right)\right) \tag{42}$$

$$\frac{d}{dt}\begin{bmatrix}\hat{\vartheta}\\ \xi\\ \hat{G}\\ \Gamma\\ \hat{H}\\ \eta\end{bmatrix} = \begin{bmatrix} k\xi \\ \left(I-\Psi\bar{D}\bar{\Psi}\right)^{-1}\left(-\Psi\bar{D}\Gamma\hat{G}-\bar{D}\xi\right) \\ -\omega_l\hat{G}+\omega_l(z-\eta)P(t) \\ \omega_r\Gamma-\omega_r\Gamma\hat{H}\Gamma \\ -\omega_l\hat{H}+\omega_l(z-\eta)N(t) \\ \omega_h(z-\eta)\end{bmatrix} \tag{43}$$

where

$$\Psi = diag\{\psi_1, \psi_2, \ldots, \psi_n\} \tag{44}$$

$$\bar{\Psi} = diag\{\bar{\psi}_1, \bar{\psi}_2, \ldots, \bar{\psi}_n\} \tag{45}$$

$$k = diag\{k_1, k_2, \ldots, k_n\} \tag{46}$$

$$\bar{D} = diag\{d_1, d_2, \ldots, d_n\} \tag{47}$$

$$D(s) = diag\left\{\frac{d_1}{s+d_1}, \frac{d_2}{s+d_2}, \ldots, \frac{d_n}{s+d_n}\right\} \tag{48}$$

$$P(t) = \left[\frac{2}{\alpha_1}\sin\omega_1 t \quad \frac{2}{\alpha_2}\sin\omega_2 t \quad \ldots \quad \frac{2}{\alpha_n}\sin\omega_n t\right]^T \tag{49}$$

$$Q(t) = \left[\alpha_1\sin\omega_1 t \quad \alpha_2\sin\omega_2 t \quad \ldots \quad \alpha_n\sin\omega_n t\right]^T \tag{50}$$

$$N(t) = \begin{bmatrix} N_{11}(t) & N_{12}(t) & \ldots & N_{1n}(t) \\ N_{12}(t) & N_{22}(t) & \ldots & N_{2n}(t) \\ \vdots & \vdots & & \vdots \\ N_{1n}(t) & N_{2n}(t) & \ldots & N_{nn}(t)\end{bmatrix} \tag{51}$$

with $N_{ii}(t) = \frac{16}{\alpha_i^2}\left(\sin^2(\omega_i t) - \frac{1}{2}\right)$ and

$$N_{ij}(t) = \frac{4}{\alpha_i\alpha_j}\sin(\omega_i t)\sin\left(\omega_j t\right), \quad (i \neq j)$$

The parameters d_i, ψ_i, and $\bar{\psi}_i$ are positive constants that are selected to satisfy $1 - \psi_i d_i \bar{\psi}_i > 0$; α_i is a small positive constant; k_i is the positive control gain; ω_i is the probing frequency, which varies for different control inputs; and ω_l, ω_h, and ω_r are the positive filter coefficients. These parameters can be written as $\omega_i = \omega\omega_i'$, $\omega_l = \omega\delta\omega_L'$, $\omega_r = \omega\delta\omega_R'$, $\omega_h = \omega\delta\omega_H'$, $\bar{D} = \omega\delta\tilde{D}$, $k = \omega\delta K'$, where ω and δ are small positive constants. Consider $\tau = \omega t$, $\tilde{\vartheta} = \hat{\vartheta} - \vartheta^*$, $\tilde{\eta} = \eta - \tilde{h}(\vartheta^*)$, $\tilde{\Gamma} = \Gamma - H^{-1}$, $\tilde{H} = \hat{H} - H$, and new perturbation signals $\tilde{P}(\tau) = P(t/\omega)$, $\tilde{Q}(\tau) = Q(t/\omega)$, $\tilde{N}(\tau) = N(t/\omega)$. The control system can be converted to the following forms

$$\omega\frac{dx}{d\tau} = f\left(x, \varphi\left(\vartheta^* + \tilde{\vartheta} + \tilde{Q}(\tau)\right)\right) \tag{52}$$

$$\frac{d}{d\tau}\begin{bmatrix}\tilde{\vartheta}\\ \xi\\ \hat{G}\\ \tilde{\Gamma}\\ \tilde{H}\\ \tilde{\eta}\end{bmatrix} = \delta\begin{bmatrix} K'\xi \\ \left(I-\omega\delta\Psi\tilde{D}\bar{\Psi}\right)^{-1}\left(-\Psi\tilde{D}\left(\tilde{\Gamma}+H^{-1}\right)\hat{G}-\tilde{D}\xi\right) \\ -\omega_L'\hat{G}+\omega_L'\left(z-\tilde{\eta}-\tilde{h}(\vartheta^*)\right)\tilde{P}(\tau) \\ \omega_R'\left(\tilde{\Gamma}+H^{-1}\right)\left(I-\left(H+\tilde{H}\right)\left(\tilde{\Gamma}+H^{-1}\right)\right) \\ -\omega_L'\left(H+\tilde{H}\right)+\omega_L'\left(z-\tilde{\eta}-\tilde{h}(\vartheta^*)\right)\tilde{N}(\tau) \\ \omega_H'\left(z-\tilde{\eta}-\tilde{h}(\vartheta^*)\right)\end{bmatrix} \tag{53}$$

To further investigated the stability of this control system, we freeze x at its equilibrium value $x = \chi\left(\vartheta^* + \tilde{\vartheta} + \tilde{Q}(\tau)\right)$, and the reduce system can be then

written as

$$\frac{d}{d\tau}\begin{bmatrix}\tilde{\vartheta}_r\\ \xi_r\\ \widehat{G}_r\\ \tilde{\Gamma}_r\\ \tilde{H}_r\\ \tilde{\eta}_r\end{bmatrix} = \delta\begin{bmatrix} K'\xi_r \\ \left(I-\omega\delta\Psi\tilde{D}\bar{\Psi}\right)^{-1}\left(-\Psi\tilde{D}\left(\tilde{\Gamma}_r+H^{-1}\right)\widehat{G}_r-\tilde{D}\xi_r\right) \\ -\omega_L'\widehat{G}_r+\omega_L'\left(v\left(\tilde{\vartheta}_r+\tilde{Q}(\tau)\right)-\tilde{\eta}_r\right)\tilde{P}(\tau) \\ \omega_R'\left(\tilde{\Gamma}_r+H^{-1}\right)\left(I-\left(H+\tilde{H}_r\right)\left(\tilde{\Gamma}_r+H^{-1}\right)\right) \\ -\omega_L'\left(H+\tilde{H}_r\right)+\omega_L'\left(v\left(\tilde{\vartheta}_r+\tilde{Q}(\tau)\right)-\tilde{\eta}_r\right)\tilde{N}(\tau) \\ \omega_H'\left(v\left(\tilde{\vartheta}_r+\tilde{Q}(\tau)\right)-\tilde{\eta}_r\right)\end{bmatrix} \tag{54}$$

where $v(\Delta)=\tilde{h}(\vartheta^*+\Delta)-\tilde{h}(\vartheta^*)$, $\Delta=\tilde{\vartheta}_r+\tilde{Q}(\tau)$. For this function, we have $v(0)=0$, $\frac{\partial v(0)}{\partial\Delta}=0$, $\frac{\partial^2 v(0)}{\partial\Delta^2}=H>0$.

By taking the common period of the probing frequencies Π as

$$\Pi = LCM\left\{\frac{1}{\omega_i'}\right\}\times 2\pi,\quad i\in\{1,2,\cdots,n\} \tag{55}$$

where LCM stands for the least common multiple, and we can derived the average model as

$$\frac{d}{d\tau}\begin{bmatrix}\tilde{\vartheta}_r^a\\ \xi_r^a\\ \widehat{G}_r^a\\ \tilde{\Gamma}_r^a\\ \tilde{H}_r^a\\ \tilde{\eta}_r^a\end{bmatrix} = \delta\begin{bmatrix} K'\xi_r^a \\ \left(I-\omega\delta\Psi\tilde{D}\bar{\Psi}\right)^{-1}\left(-\Psi\bar{D}\left(\tilde{\Gamma}_r^a+H^{-1}\right)\widehat{G}_r^a-\tilde{D}\xi_r^a\right) \\ -\omega_L'\widehat{G}_r^a+\frac{\omega_L'}{\Pi}\int_0^\Pi v\left(\tilde{\vartheta}_r^a+\tilde{Q}(\sigma)\right)\tilde{P}(\sigma)\,d\sigma \\ \omega_R'\left(\tilde{\Gamma}_r^a+H^{-1}\right)\left(I-\left(H+\tilde{H}_r^a\right)\left(\tilde{\Gamma}_r^a+H^{-1}\right)\right) \\ -\omega_L'\left(H+\tilde{H}_r^a\right)+\frac{\omega_L'}{\Pi}\int_0^\Pi v\left(\tilde{\vartheta}_r^a+\tilde{Q}(\sigma)\right)\tilde{N}(\sigma)\,d\sigma \\ -\omega_H'\tilde{\eta}_r^a+\frac{\omega_H'}{\Pi}\int_0^\Pi v\left(\tilde{\vartheta}_r^a+\tilde{Q}(\sigma)\right)d\sigma\end{bmatrix} \tag{56}$$

The average equilibrium $(\tilde{\vartheta}_r^{a,e}, \xi_r^{a,e}, \widehat{G}_r^{a,e}, \tilde{\Gamma}_r^{a,e}, \tilde{H}_r^{a,e}, \tilde{\eta}_r^{a,e})$ satisfies

$$\xi_r^{a,e}=0_{n\times 1} \tag{57}$$

$$\widehat{G}_r^{a,e}=0_{n\times 1} \tag{58}$$

$$\int_0^\Pi v\left(\tilde{\vartheta}_r^{a,e}+\tilde{Q}(\sigma)\right)\tilde{P}(\sigma)\,d\sigma=0_{n\times 1} \tag{59}$$

$$\tilde{\eta}_r^{a,e}=\frac{1}{\Pi}\int_0^\Pi v\left(\tilde{\vartheta}_r^{a,e}+\tilde{Q}(\sigma)\right)d\sigma \tag{60}$$

$$H+\tilde{H}_r^{a,e}=\frac{1}{\Pi}\int_0^\Pi v\left(\tilde{\vartheta}_r^{a,e}+\tilde{Q}(\sigma)\right)\tilde{N}(\sigma)\,d\sigma \tag{61}$$

$$I=\left(H+\tilde{H}_r^{a,e}\right)\left(\tilde{\Gamma}_r^{a,e}+H^{-1}\right) \tag{62}$$

For small α_i, $\tilde{\Gamma}_r^{a,e}+H^{-1}>0$. With a Taylor expansion of (59), we get

$$\begin{aligned}\int_0^\Pi\Bigg(&\frac{1}{2}\sum_{i=1}^n\sum_{j=1}^n\frac{\partial v(0)}{\partial\Delta_i\partial\Delta_j}\\ &\times\left(\tilde{\vartheta}_{r,i}^{a,e}+\alpha_i\sin\left(\omega_i'\varsigma\right)\right)\left(\tilde{\vartheta}_{r,j}^{a,e}+\alpha_j\sin\left(\omega_j'\varsigma\right)\right)\\ &+\frac{1}{3!}\sum_{i=1}^n\sum_{j=1}^n\sum_{k=1}^n\frac{\partial^3 v(0)}{\partial\Delta_i\partial\Delta_j\partial\Delta_k}\left(\tilde{\vartheta}_{r,i}^{a,e}+\alpha_i\sin\left(\omega_i'\varsigma\right)\right)\\ &\times\left(\tilde{\vartheta}_{r,j}^{a,e}+\alpha_j\sin\left(\omega_j'\varsigma\right)\right)\left(\tilde{\vartheta}_{r,k}^{a,e}+\alpha_k\sin\left(\omega_k'\varsigma\right)\right)+O\left(|\alpha|^4\right)\Bigg)\\ &\times\frac{2}{\alpha_p}\sin\left(\omega_p'\varsigma\right)d\varsigma=0,\forall p\in\{1,2,\cdots,n\}\end{aligned} \tag{63}$$

Define

$$\tilde{\vartheta}_{r,i}^{a,e}=\sum_{j=1}^n b_j^i\alpha_j+\sum_{j=1}^n\sum_{k=1}^n c_{j,k}^i\alpha_j\alpha_k+O\left(|\alpha|^3\right) \tag{64}$$

where b_j^i and $c_{j,k}^i$ are real numbers. Substituting $\tilde{\vartheta}_{r,i}^{a,e}$ and $\left(\tilde{\vartheta}_{r,i}^{a,e}\right)^2$ to (65) and matching the like power of α_j, we have

$$\begin{bmatrix}\frac{\partial^2 v(0)}{\partial\Delta_1\partial\Delta_1} & \cdots & \frac{\partial^2 v(0)}{\partial\Delta_1\partial\Delta_n}\\ \vdots & \vdots & \vdots\\ \frac{\partial^2 v(0)}{\partial\Delta_n\partial\Delta_1} & \cdots & \frac{\partial^2 v(0)}{\partial\Delta_n\partial\Delta_n}\end{bmatrix}\begin{bmatrix}b_j^1\\ \vdots\\ b_j^n\end{bmatrix}=H\begin{bmatrix}b_j^1\\ \vdots\\ b_j^n\end{bmatrix}=\begin{bmatrix}0\\ \vdots\\ 0\end{bmatrix} \tag{65}$$

Hence, for all $i,j\in\{1,2,\cdots,n\}$, we can obtain $b_j^i=0$. Next, matching the like power of $\alpha_k\alpha_l$, $(k\neq l)$, we have

$$\begin{bmatrix}\frac{\partial^2 v(0)}{\partial\Delta_1\partial\Delta_1} & \cdots & \frac{\partial^2 v(0)}{\partial\Delta_1\partial\Delta_n}\\ \vdots & \vdots & \vdots\\ \frac{\partial^2 v(0)}{\partial\Delta_n\partial\Delta_1} & \cdots & \frac{\partial^2 v(0)}{\partial\Delta_n\partial\Delta_n}\end{bmatrix}\begin{bmatrix}c_{k,l}^1\\ \vdots\\ c_{k,l}^n\end{bmatrix}=H\begin{bmatrix}c_{k,l}^1\\ \vdots\\ c_{k,l}^n\end{bmatrix}=\begin{bmatrix}0\\ \vdots\\ 0\end{bmatrix} \tag{66}$$

Similarly, we can obtain $c^i_{k,l} = 0$. Finally, matching the like power of α_l^2, $(k = l)$, we have

$$H\begin{bmatrix} c^1_{l,l} \\ \vdots \\ c^{l-1}_{l,l} \\ c^l_{l,l} \\ c^{l+1}_{l,l} \\ \vdots \\ c^n_{l,l} \end{bmatrix} + \frac{1}{4}\begin{bmatrix} \frac{\partial^3 v(0)}{\partial \Delta_l^2 \partial \Delta_1} \\ \vdots \\ \frac{\partial^3 v(0)}{\partial \Delta_l^2 \partial \Delta_{l-1}} \\ \frac{1}{2}\frac{\partial^3 v(0)}{\partial \Delta_l^3} \\ \frac{\partial^3 v(0)}{\partial \Delta_l^2 \partial \Delta_{l+1}} \\ \vdots \\ \frac{\partial^3 v(0)}{\partial \Delta_l^2 \partial \Delta_n} \end{bmatrix} = \begin{bmatrix} 0 \\ \vdots \\ 0 \\ 0 \\ 0 \\ \vdots \\ 0 \end{bmatrix} \Rightarrow \begin{bmatrix} c^1_{l,l} \\ \vdots \\ c^{l-1}_{l,l} \\ c^l_{l,l} \\ c^{l+1}_{l,l} \\ \vdots \\ c^n_{l,l} \end{bmatrix}$$

$$= -\frac{1}{4}H^{-1}\begin{bmatrix} \frac{\partial^3 v(0)}{\partial \Delta_l^2 \partial \Delta_1} \\ \vdots \\ \frac{\partial^3 v(0)}{\partial \Delta_l^2 \partial \Delta_{l-1}} \\ \frac{1}{2}\frac{\partial^3 v(0)}{\partial \Delta_l^3} \\ \frac{\partial^3 v(0)}{\partial \Delta_l^2 \partial \Delta_{l+1}} \\ \vdots \\ \frac{\partial^3 v(0)}{\partial \Delta_l^2 \partial \Delta_n} \end{bmatrix} \tag{67}$$

According to above, we can get

$$\tilde{\vartheta}^{a,e}_{r,i} = \sum_{l=1}^{n} c^i_{l,l}\alpha_l^2 + O\left(|\alpha|^3\right) \tag{68}$$

Moreover, with a Taylor expansion of (60) and (61), we have

$$\begin{aligned}
&\tilde{\eta}^{a,e}_r \\
&= \frac{1}{\Pi}\int_0^{\Pi}\Bigg[\frac{1}{2}\sum_{i=1}^{n}\sum_{j=1}^{n}\frac{\partial^2 v(0)}{\partial\Delta_i\partial\Delta_j}\left(\tilde{\vartheta}^{a,e}_{ri} + \alpha_i\sin\left(\omega_i'\varsigma\right)\right) \\
&\quad\times\left(\tilde{\vartheta}^{a,e}_{rj} + \alpha_j\sin\left(\omega_j'\varsigma\right)\right) + \frac{1}{3!}\sum_{i=1}^{n}\sum_{j=1}^{n}\sum_{k=1}^{n}\frac{\partial^3 v(0)}{\partial\Delta_i\partial\Delta_j\partial\Delta_k} \\
&\quad\times\left(\tilde{\vartheta}^{a,e}_{ri} + \alpha_i\sin\left(\omega_i'\varsigma\right)\right)\left(\tilde{\vartheta}^{a,e}_{rj} + \alpha_j\sin\left(\omega_j'\varsigma\right)\right) \\
&\quad\times\left(\tilde{\vartheta}^{a,e}_{rk} + \alpha_k\sin\left(\omega_k'\varsigma\right)\right) + \mathrm{O}\left(|\alpha|^4\right)\Bigg]d\varsigma
\end{aligned} \tag{69}$$

$$\begin{aligned}
&\left(\tilde{H}^{a,e}_r\right)_{p,p} + H_{p,p} \\
&= \frac{1}{\Pi}\int_0^{\Pi}\Bigg[\frac{1}{2}\sum_{i=1}^{n}\sum_{j=1}^{n}\frac{\partial^2 v(0)}{\partial\Delta_i\partial\Delta_j}\left(\tilde{\vartheta}^{a,e}_{r,i} + \alpha_i\sin\left(\omega_i'\varsigma\right)\right) \\
&\quad\times\left(\tilde{\vartheta}^{a,e}_{r,j} + \alpha_j\sin\left(\omega_j'\varsigma\right)\right) + \frac{1}{3!}\sum_{i=1}^{n}\sum_{j=1}^{n}\sum_{k=1}^{n}\frac{\partial^3 v(0)}{\partial\Delta_i\partial\Delta_j\partial\Delta_k} \\
&\quad\times\left(\tilde{\vartheta}^{a,e}_{r,i} + \alpha_i\sin\left(\omega_i'\varsigma\right)\right)\left(\tilde{\vartheta}^{a,e}_{r,j} + \alpha_j\sin\left(\omega_j'\varsigma\right)\right) \\
&\quad\times\left(\tilde{\vartheta}^{a,e}_{r,k} + \alpha_k\sin\left(\omega_k'\varsigma\right)\right) \\
&\quad+\mathrm{O}\left(|\alpha|^4\right)\Bigg]\times\frac{16}{\alpha_p^2}\left(\sin^2\left(\omega_p'\varsigma\right) - \frac{1}{2}\right)d\varsigma, \\
&\quad\forall p \in \{1, 2, \cdots, n\}
\end{aligned} \tag{70}$$

$$\begin{aligned}
&\left(\tilde{H}^{a,e}_r\right)_{p,m} + H_{p,m} \\
&= \frac{1}{\Pi}\int_0^{\Pi}\Bigg[\frac{1}{2}\sum_{i=1}^{n}\sum_{j=1}^{n}\frac{\partial^2 v(0)}{\partial\Delta_i\partial\Delta_j}\left(\tilde{\vartheta}^{a,e}_{ri} + \alpha_i\sin\left(\omega_i'\varsigma\right)\right) \\
&\quad\times\left(\tilde{\vartheta}^{a,e}_{rj} + \alpha_j\sin\left(\omega_j'\varsigma\right)\right) + \frac{1}{3!}\sum_{i=1}^{n}\sum_{j=1}^{n}\sum_{k=1}^{n}\frac{\partial^3 v(0)}{\partial\Delta_i\partial\Delta_j\partial\Delta_k} \\
&\quad\times\left(\tilde{\vartheta}^{a,e}_{ri} + \alpha_i\sin\left(\omega_i'\varsigma\right)\right)\left(\tilde{\vartheta}^{a,e}_{rj} + \alpha_j\sin\left(\omega_j'\varsigma\right)\right) \\
&\quad\left(\tilde{\vartheta}^{a,e}_{rk} + \alpha_k\sin\left(\omega_k'\varsigma\right)\right) \\
&\quad+\mathrm{O}\left(|\alpha|^4\right)\Bigg]\frac{4}{\alpha_p\alpha_m}\sin\left(\omega_p' t\right)\sin\left(\omega_m' t\right)d\varsigma, \\
&\quad\forall p, m \in \{1, 2, \cdots, n\}, \quad p \neq m
\end{aligned} \tag{71}$$

Substituting $\tilde{\vartheta}^{a,e}_{r,i}$ to (69), (70) and (71), $\tilde{\eta}^{a,e}_r$ and $\tilde{H}^{a,e}_r$ can be expressed as

$$\tilde{\eta}^{a,e}_r = \frac{1}{4}\sum_{i=1}^{n}H_{i,i}\alpha_i^2 + O\left(|\alpha|^3\right) \tag{72}$$

$$\left(\tilde{H}^{a,e}_r\right)_{p,p} = \sum_{i=1}^{n}\frac{\partial^3 v(0)}{\partial\Delta_i\partial\Delta_p^2}\tilde{\vartheta}^{a,e}_{r,i} \tag{73}$$

$$\left(\tilde{H}^{a,e}_r\right)_{p,m} = \sum_{i=1}^{n}\frac{\partial^3 v(0)}{\partial\Delta_i\partial\Delta_p\partial\Delta_m}\tilde{\vartheta}^{a,e}_{r,i} \tag{74}$$

$$\tilde{H}^{a,e}_r = \sum_{i=1}^{n}\sum_{j=1}^{n}\Theta^i c^i_{j,j}\alpha_j^2 + \left(O\left(|\alpha|^3\right)\right)_{n\times n} \tag{75}$$

where Θ^i is a $n \times n$ matrix with

$$\left(\Theta^i\right)_{p,m} = \frac{\partial^3 v(0)}{\partial\Delta_i\partial\Delta_p\partial\Delta_m} \tag{76}$$

Substituting $\tilde{\vartheta}^{a,e}_{r,i}$ to (62), $\tilde{\Gamma}^{a,e}_r$ can be written as

$$\begin{aligned}
\tilde{\Gamma}^{a,e}_r &= \left(H\left(H^{-1}\tilde{H}^{a,e}_r + I\right)\right)^{-1} - H^{-1} \\
&= -\sum_{i=1}^{n}\sum_{j=1}^{n}H^{-1}\Theta^i H^{-1}c^i_{j,j}\alpha_j^2 + \left[\mathrm{O}\left(|\alpha|^3\right)\right]_{n\times n}
\end{aligned} \tag{77}$$

The Jacobian of (56) is expressed as

$$J^{a,e}_r = \delta\begin{bmatrix} A_{3n\times 3n} & 0_{3n\times(2n+1)} \\ B_{(2n+1)\times 3n} & D_{(2n+1)\times(2n+1)} \end{bmatrix} \tag{78}$$

where

$$\begin{aligned}
&A_{3n\times 3n} \\
&= \begin{bmatrix} 0_{n\times n} & K' & 0_{n\times n} \\ 0_{n\times n} & -\left(I - \omega\delta\Psi\tilde{D}\bar{\Psi}\right)^{-1}\tilde{D} & A_{23} \\ A_{31} & 0_{n\times n} & -\omega_L' I_{n\times n} \end{bmatrix}
\end{aligned} \tag{79}$$

$$B_{(2n+1)\times 3n} = \begin{bmatrix} 0_{n\times n} & 0_{n\times n} & 0_{n\times n} \\ \frac{\omega_L'}{\Pi}\int_0^{\Xi}\frac{\partial}{\partial\tilde{\vartheta}}\left(v\tilde{N}(\varsigma)\right)d\varsigma & 0_{n\times n} & 0_{n\times n} \\ \frac{\omega_H'}{\Pi}\int_0^{\Pi}\frac{\partial}{\partial\tilde{\vartheta}}(v)\,d\varsigma & 0_{n\times n} & 0_{n\times n} \end{bmatrix} \tag{80}$$

$$D_{(2n+1)\times(2n+1)} = \begin{bmatrix} -\omega_R' I_{n\times n} & -\omega_R' H^{-1}+\Lambda_1 & 0_{n\times n} \\ 0_{n\times n} & -\omega_L' I_{n\times n} & 0_{n\times n} \\ 0_{1\times n} & 0_{1\times n} & -\omega_H' \end{bmatrix} \tag{81}$$

with

$$A_{23} = -\left(I-\omega\delta\Psi\tilde{D}\bar{\Psi}\right)^{-1}\Psi\tilde{D}\left(\tilde{\Gamma}_r^{a,e}+H^{-1}\right) \tag{82}$$

$$A_{31} = \frac{\omega_L'}{\Pi}\int_0^{\Pi}\frac{\partial}{\partial\tilde{\vartheta}}\left(v\tilde{P}(\varsigma)\right)d\varsigma = \omega_L' H + O(|\alpha|) \tag{83}$$

$$\Lambda_1 = \breve{\omega}_R\sum_{i=1}^{n}\sum_{h=1}^{n}H^{-1}\left(\Omega^i H^{-1}+H^{-1}\Omega^i\right)H^{-1}c_{hh}^i\alpha_h^2 + \left[O\left(|\alpha|^3\right)\right]_{n\times n} \tag{84}$$

Since $A_{31} > 0$, $\omega_L', \omega_R', \omega_H' > 0$, $I-\omega\delta\Psi\tilde{D}\bar{\Psi} > 0$ and $\tilde{\Gamma}_r^{a,e}+H^{-1} > 0$, it is proved that $J_r^{a,e}$ is Hurwitz for sufficiently small α_i. Hence, there exist $\bar{\delta}$, $\bar{\alpha}$ such that for all $\alpha \in (0,\bar{\alpha})$ and $\delta \in (0,\bar{\delta})$ the reduced system (54) has a unique exponentially stable periodic solution $(\tilde{\vartheta}_r^{\Pi}, \xi_r^{\Pi}, \widehat{G}_r^{\Pi}, \tilde{\Gamma}_r^{\Pi}, \tilde{H}_r^{\Pi}, \tilde{\eta}_r^{\Pi})$ of period Π and this solution satisfies

$$\left|\tilde{\vartheta}_{r,i}^{\Pi}-\sum_{j=1}^{n}c_{j,j}^i\alpha_j^2\right| \le O\left(\delta+|\alpha|^3\right) \tag{85}$$

$$\left|\xi_r^{\Pi}\right| \le O\left(\delta+|\alpha|^3\right) \tag{86}$$

$$\left|\widehat{G}_r^{\Pi}\right| \le O\left(\delta+|\alpha|^3\right) \tag{87}$$

$$\left|\tilde{\Gamma}_r^{\Pi}+\sum_{i=1}^{n}\sum_{j=1}^{n}H^{-1}\Theta^i H^{-1}c_{j,j}^i\alpha_j^2\right| \le O\left(\delta+|\alpha|^3\right) \tag{88}$$

$$\left|\tilde{H}_r^{\Pi}-\sum_{i=1}^{n}\sum_{j=1}^{n}\Theta^i c_{j,j}^i\alpha_j^2\right| \le O\left(\delta+|\alpha|^3\right) \tag{89}$$

$$\left|\tilde{\eta}_r^{\Pi}-\frac{1}{4}\sum_{i=1}^{n}H_{i,i}\alpha_i^2\right| \le O\left(\delta+|\alpha|^3\right) \tag{90}$$

The control system based on multivariate ES-NM is demonstrated to be asymptotically stable. Additionally, the choice of control parameters is discussed here. As shown in Fig. 3, the gain matrix k has a great effect on the convergence speed of the control system. The convergence will be very slow if k is too small, but a too large k will lead to severe oscillation or instability. The value of k should be large enough in a suitable range. ω_l is the coefficient of the high pass filter. It is required to be large enough. Oppositely, ω_h is the coefficient of the low pass filter. It is required to be small enough. ω_r is used to construct the estimates of H^{-1}.

FIGURE 4. Flight test for the parafoil-UAV system.

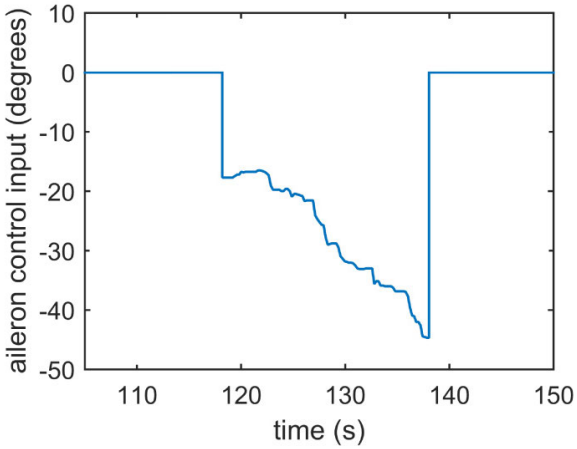

FIGURE 5. Aileron control input in flight test.

TABLE 2. System geometric parameters.

Parameter	Parafoil	UAV
Mass, kg	2.5	8
b, m	4.5	2.1
c, m	1.6	0.36
AR	2.8	5.8
S, m^2	7.2	0.76

It is required to satisfy $\omega_r > 0$. For the probing frequencies, they are required to satisfy $\omega_i \neq \omega_j$ and $\omega_i+\omega_j \neq \omega_k$ for $i \neq j \neq k$. The further investigation of control parameters is shown in [16], [28].

IV. FLIGHT TEST

The reliability of the control performance evaluation and the accuracy of the control parameter estimation depend on the precision of the proposed model that is related to the parafoil and UAV aerodynamic coefficients. To improve the precision of the model, a flight test was conducted in June, 2019. The test system contains a 2.5 kg rectangular parafoil and an 8 kg fixed-wing UAV, as shown in Fig. 4. The detailed geometric parameters of this test system are listed in Table 2. For the

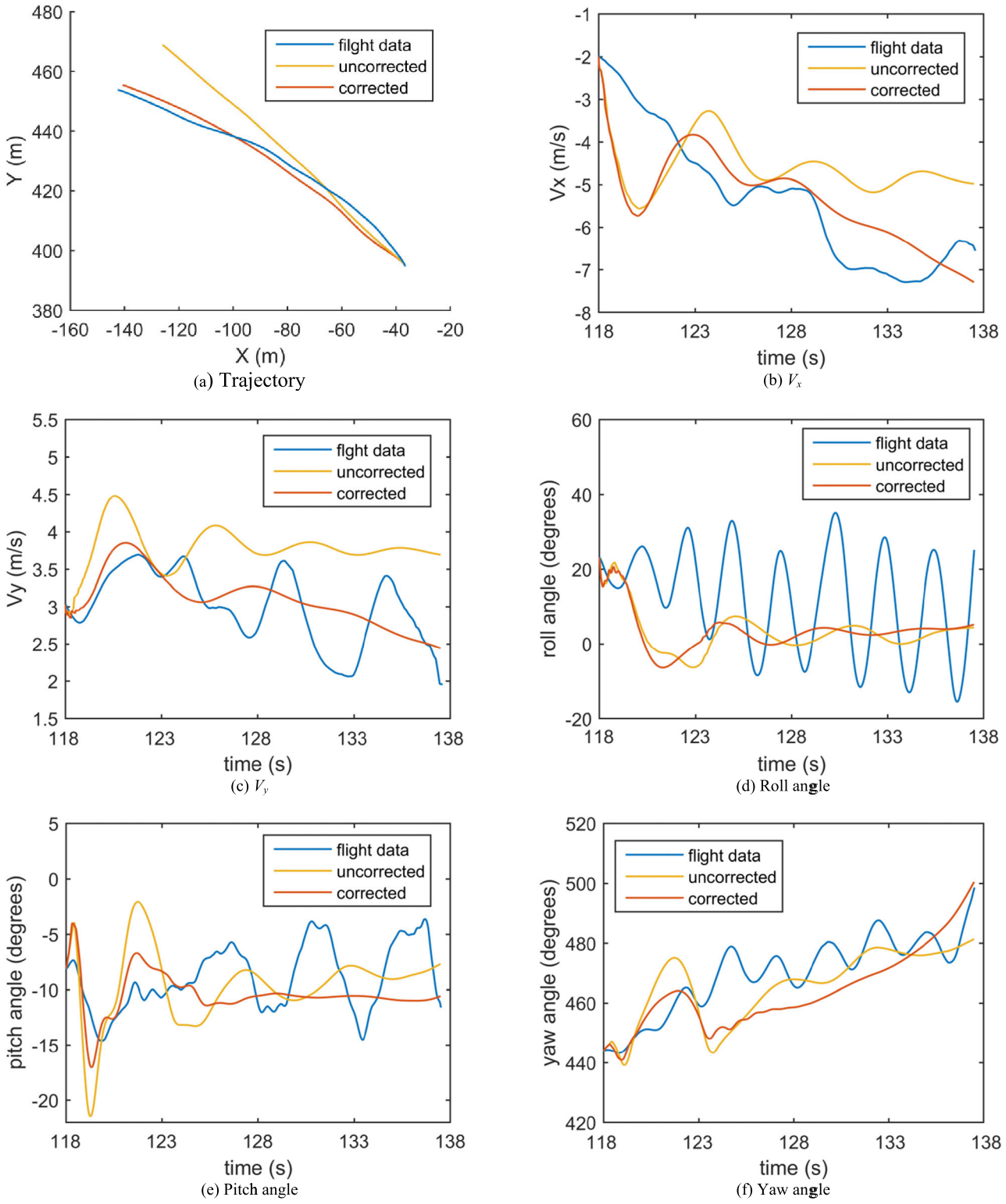

FIGURE 6. Comparisons of the flight test and simulation.

parafoil, the span length is 4.5 m, the chord length is 1.6 m, and the canopy area is 7.2 m^2. For the UAV, the span length is 2.1 m, the chord length is 0.36 m, and the wing area is 0.76 m^2. The wing, flat tail and vertical tail of this UAV are equipped with an aileron, an elevator and a rudder that can be manipulated during flight. In this test, the average

TABLE 3. Parafoil aerodynamic coefficients.

parameter	value	parameter	value	parameter	value
C_{L0}	0.04	$C_{y\beta}$	-0.26	$C_{L\delta s}$	0.21
$C_{L\alpha}$	4.4	$C_{l\beta}$	0.102	$C_{D\delta s}$	0.3
C_{D0}	0.16	C_{lp}	-0.15	$C_{l\delta a}$	-0.00128
$C_{D\alpha^2}$	5.8	C_{lr}	0	$C_{n\delta a}$	0.012
C_{m0}	-0.12	$C_{n\beta}$	0.047		
$C_{m\alpha}$	-1	C_{np}	0		
C_{mq}	-2	C_{nr}	-0.094		

wind speed is 4.57 m/s, and the average wind direction is 203 degrees. The parafoil-UAV system is released from a height of 104 m. After gilding steadily, the series of aileron control inputs shown in Fig. 5 are performed. The flight data of this test are obtained from inertial measurement unit (IMU) and global positioning system (GPS) sensors that are fixed in the fuselage of the UAV. The motion of the UAV can be observed clearly.

During the test, significant relative motion is observed between the parafoil and the UAV. This relative motion makes the aerodynamic coefficients of the parafoil-UAV system difficult to identify completely from the only known data, which are the velocity and angular velocity of the UAV. The identification of aerodynamic coefficients for this test system is not suitable. CFD is another method to calculate aerodynamic coefficients. By using CFD, Wu, Ghoreyshi and Ye [29]–[31] has been calculated the aerodynamic stability derivatives of the parafoil and the UAV, respectively. For the UAV, the calculated coefficients are reliable. However, for the parafoil, they are not accurate enough due to the canopy geometric deformation. The aerodynamic coefficients of the parafoil need to be corrected.

Substituting all aerodynamic coefficients calculated via CFD into the model and running the simulation, the simulation result of the uncorrected model is obtained. As shown in Fig. 6, significant errors exist between the simulation results and the test data, which are mainly caused by the inaccurate aerodynamic coefficients and the unknown wind variation during the test. To minimize the errors and improve the precision of the model, the static and dynamic stability derivatives of the parafoil are artificially adjusted within a reasonable range. Compared with the uncorrected model, the corrected model can well capture the basic motions of the test system. All corrected aerodynamic coefficients are listed in Tables 3 and 4.

V. SIMULATION OF THE CONTROL PERFORMANCE

To study the performance of the multivariate ES-NM controller, a new parafoil-UAV system is designed. The shape of the parafoil remains unchanged, while the size of the UAV is increased proportionally. According to the similarity

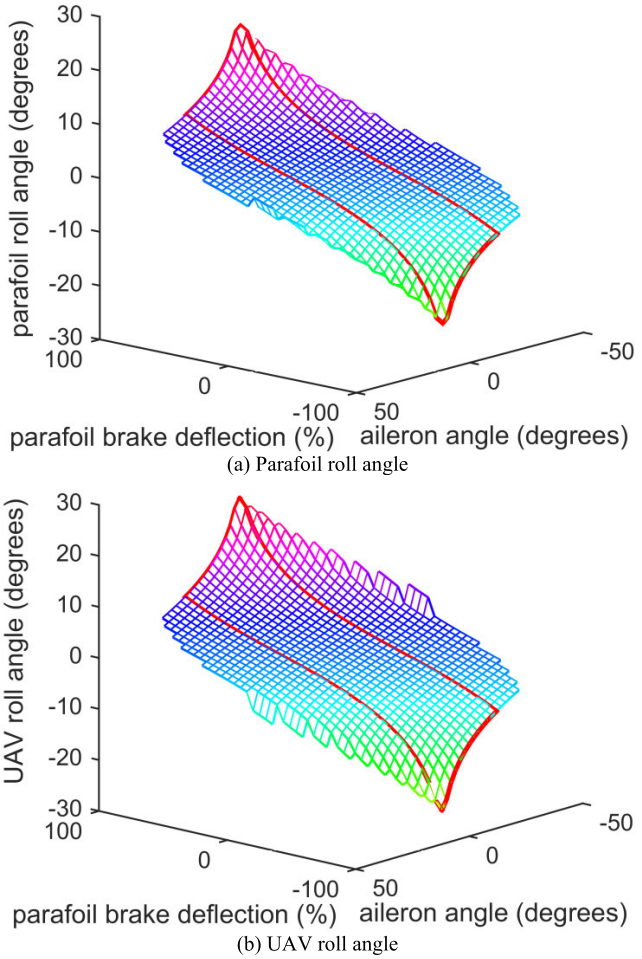

FIGURE 7. Roll angles under varying parafoil brake defections and UAV aileron control.

theory of aerodynamics, the parafoil and UAV aerodynamic coefficients of this new system can be considered the same as those of the flight test system mentioned above. Using the detailed geometric parameters listed in Table 5, the multibody dynamic model of this parafoil-UAV system is established and programmed in MATLAB. In this section, this model is used to analyze the influence of the parafoil and UAV control mechanisms and to assess the control performance of the proposed method. The detailed results are shown as follows.

A. CONTROL RANGE DESIGN

As mentioned above, a parafoil-UAV system has a parafoil and a UAV. Each part has its own control mechanism. The parafoil control mechanisms are the left and right deflections of the parafoil trailing edge, whereas the UAV control mechanisms are the deflections of the aileron, elevator, and rudder. The longitudinal control of this system is achieved directly by UAV elevator deflection, whereas the lateral control is achieved by parafoil brake deflection together with aileron and rudder deflection of the UAV. These two control mechanisms interfere with each other and have a great influence on the controllability and stability of the parafoil-UAV system.

TABLE 4. UAV aerodynamic coefficients.

C^b_{L0}	$C^b_{L\alpha}$	$C^b_{L\delta e}$	$C^b_{L\dot{\alpha}}$	C^b_{Lq}	C^b_{D0}	$C^b_{D\delta e}$	$C^b_{D\delta a}$
0.062	5.195	0.2167	1.22	4.589	0.028	0.0418	0
$C^b_{D\delta r}$	$C^b_{y\beta}$	$C^b_{y\delta a}$	$C^b_{y\delta r}$	C^b_{yp}	C^b_{yr}	$C^b_{l\beta}$	C^b_{lp}
0	-0.2083	0.0	0.1096	0.0057	0.0645	-0.0339	-0.4243
C^b_{lr}	$C^b_{l\delta a}$	$C^b_{l\delta r}$	C^b_{m0}	$C^b_{m\alpha}$	$C^b_{m\delta e}$	$C^b_{m\dot{\alpha}}$	C^b_{mq}
0.0288	-0.2559	0.0085	-0.30	-0.40	-0.6934	-2.897	-5.263
$C^b_{n\beta}$	C^b_{np}	C^b_{nr}	$C^b_{n\delta a}$	$C^b_{n\delta r}$			
0.0116	-0.0076	-0.0276	-0.0068	-0.0515			

TABLE 5. System geometric parameters.

Parameter	Parafoil	UAV
Mass, kg	2.5	15
b, m	4.5	2.94
c, m	1.6	0.51
AR	2.8	5.8
S, m^2	7.2	1.5

Hence, before designing an optimal controller, it is necessary to use the dynamic model to analyze the interaction effect of the two control mechanisms and redesign the control range of the parafoil-UAV system.

Fig. 7 shows the steady-state roll angles of the parafoil and UAV with varying parafoil brake deflections and UAV aileron deflections. The parafoil brake deflection changes from −100% to 100%, and the UAV aileron deflection changes from −40 to 40 degrees. Under −100% parafoil brake deflection and 12-degree aileron deflection, the parafoil and UAV roll angles are minimal. The parafoil roll angle is −21.3 degrees, and the UAV roll angle is −23.3 degrees. In contrast, under 100% parafoil brake deflection and −12-degree aileron deflection, the parafoil and UAV roll angles are maximal. Compared with a system controlled by a single mechanism, the system controlled by two mechanisms can perform flight maneuvers with larger roll angles and smaller turning radii. On the other hand, the parafoil brake deflection has a great influence on the control range of the UAV aileron permitted by the parafoil-UAV system. When the parafoil brake deflection is −100%, the minimum aileron deflection that the system permits is −22 degrees, the maximum aileron deflection is 12 degrees, and the aileron control range is −22 to 12 degrees. When the parafoil brake deflection increases to 0%, the minimum aileron deflection decreases and the maximum deflection increases. The aileron control range is −28 to 28 degrees, which is larger than the previous range. When the parafoil brake deflection increases to 100%, the aileron control range is −12 to 22 degrees. As the parafoil brake deflection increases, the aileron control range decreases. The aileron control range is directly related to the parafoil brake deflection. To simplify the design of the control range, in this paper, the control range of the parafoil brake deflection is set as −100 to 100%, and the control range of the UAV aileron deflection is set as −12 to 12 degrees. In this control range, the maximum and minimum roll angles of the parafoil and the UAV can be achieved.

The angle of attack is another parameter that can be used to design the control range. Fig. 8 shows the angles of attack of the parafoil and UAV under varying parafoil brake deflections (−100 to 100%) and UAV aileron deflections (−40 to 40 degrees). When both the parafoil brake deflection and the aileron deflection are 0, the parafoil and UAV angles of attack are maximized, with the angle values of 13.7 degrees and 9 degrees, respectively. When the parafoil brake deflection is 100% and the aileron deflection is −12 degrees and when the parafoil brake deflection is −100% and the aileron deflection is 12 degrees, the parafoil and UAV angles of attack are minimal, with the angle values of 6.4 degrees and 2.5 degrees, respectively. In the designed control range, the angles of attack of the parafoil and the UAV do not exceed the angle of stall. This designed control range is reasonable for the parafoil-UAV system.

Fig. 9 shows the parafoil and UAV pitch angles with varying parafoil brake deflections and UAV elevator deflections. The parafoil brake deflection changes from 0 to 100%, and the UAV elevator deflection changes from −40 to 40 degrees. When the parafoil brake deflection is zero, the parafoil pitch angle decreases from −6.2 degrees to −10.6 degrees, and the UAV pitch angle decreases from −6.2 to −21.6 degrees with increasing UAV elevator deflection. When the parafoil brake deflection is full, the parafoil pitch angle decreases from −8.9 degrees to −25.6 degrees, and the UAV pitch angle decreases from −5.7 degrees to −39.4 degrees. Although the parafoil brake deflection does not directly control the longitudinal motion, it has a great effect on the control performance of the UAV elevator.

Fig. 10 shows the angles of attack of the parafoil and UAV under varying parafoil brake deflections (0 to 100%) and UAV elevator deflections (−40 to 40 degrees). With the increase of the parafoil brake deflection and UAV elevator deflection, the angles of attack of the parafoil and UAV decrease. Under these control inputs, all angles of attack are convergent. The motion of the parafoil-UAV system is steady at all times. However, due to the angle of stall, the UAV elevator deflection also has its own limit. For the system in this paper, the parafoil angle of attack should be less than 15 degrees, the UAV angle of attack should be less than

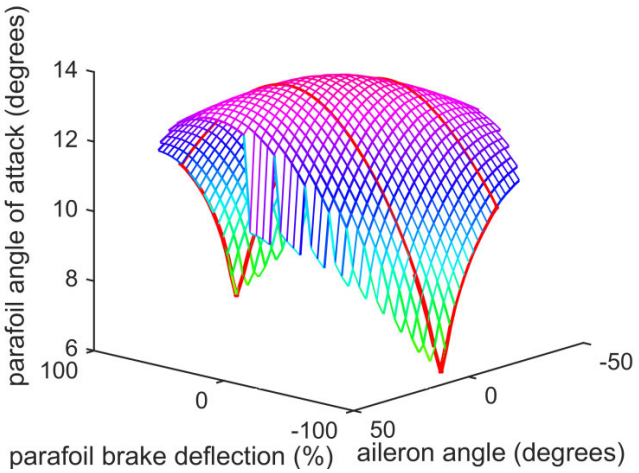

(a) Parafoil angle of attack

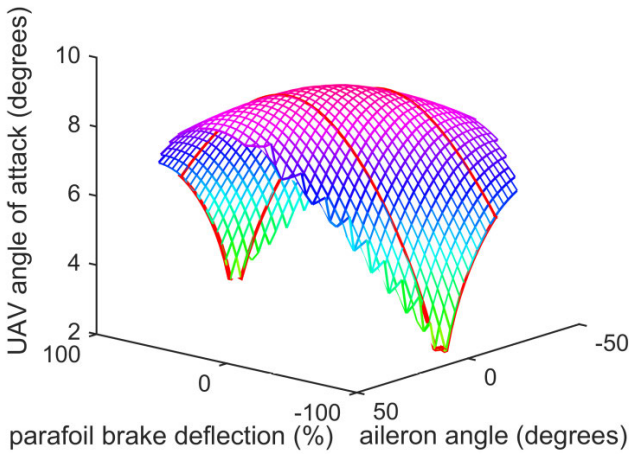

(b) UAV angle of attack

FIGURE 8. Angles of attack under varying parafoil brake defections and UAV aileron control.

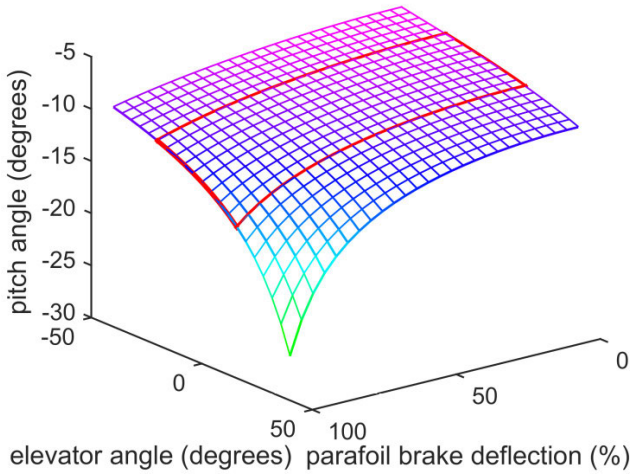

(a) Parafoil pitch angle

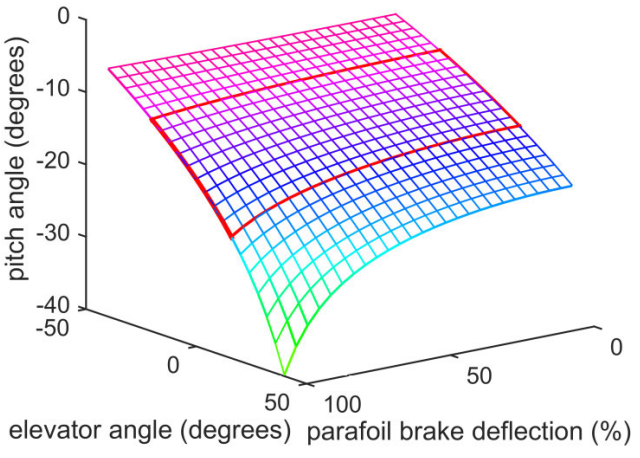

(b) UAV pitch angle

FIGURE 9. Pitch angles under varying parafoil brake defections and UAV elevator control.

13 degrees, and both of these angles need to be positive. Hence, the elevator control range can be set as -20 to 16 degrees, and the parafoil brake deflection can be set as 0 to 100%. Considering the symmetry of the parafoil brake deflection, its control range can be set as -100 to 100%.

B. SIMULATION OF THE OPTIMAL CONTROL

Using the control range, a multivariate optimal controller based on ES-NM is accomplished. To assess the control performance of the proposed method, two cases are simulated in this article.

Case 1: The parafoil brake deflection and the UAV aileron deflection are initially 50% and -5 degrees, respectively, and no wind exists.

Case 2: The parafoil brake deflection and the UAV aileron deflection are initially zero, and variable wind exists.

For these two cases, the main purpose of the controller is to make the roll angle of the UAV as close to zero as possible by using the parafoil brake deflection and the UAV aileron deflection. Hence, the cost function of the system can be written as

$$z = h(\phi_b) = 0.5(\phi_b - 0)^2 \tag{91}$$

In the multivariate ES-NM controller, the estimated input of the parafoil-UAV system $\widehat{\vartheta}$ contains the estimated parafoil brake deflection $\widehat{\delta}_a^p$ and the estimated UAV aileron deflection $\widehat{\delta}_a^b$. The control range of the parafoil brake deflection is -100 to 100%, and the range of the UAV aileron deflection is -12 to 12 degrees. The probing frequencies ω_1 and ω_2 are estimated as 5π and 4.5π, respectively. The filter coefficients ω_l, ω_r and ω_h are 500, 10^{-4} and 3, respectively. The gain matrix k is $diag\{100,\ 300\}$. The other parameters are selected as follows: $\alpha = [0.1,\ 0.1]^T$, $\bar{D} = diag\{0.01,\ 0.01\}$, $\bar{\Psi} = diag\{10,\ 10\}$, $\Psi = diag\{2,\ 3\}$, and $\Gamma_0^{-1} = 400 diag\{1,\ 1\}$.

The simulation for Case 1 is performed first, and the results are presented in Fig. 11. Under the influence of the multivariate ES-NM controller, the estimated parafoil brake deflection rapidly decreases from 50% to 0%. Meanwhile, the estimated UAV aileron deflection increases as well and converges to zero at 600 s. Correspondingly, the roll angles of the parafoil and the UAV decrease and converge to the desired attitude, as shown in Fig. 12. This demonstrates that the multivariate ES-NM controller can adjust the two control

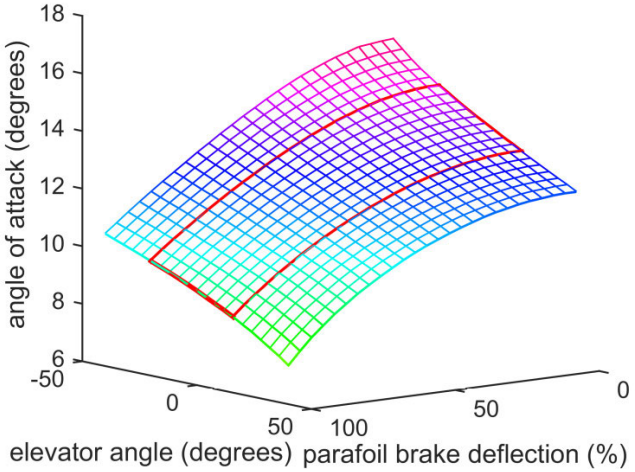

(a) Parafoil angle of attack

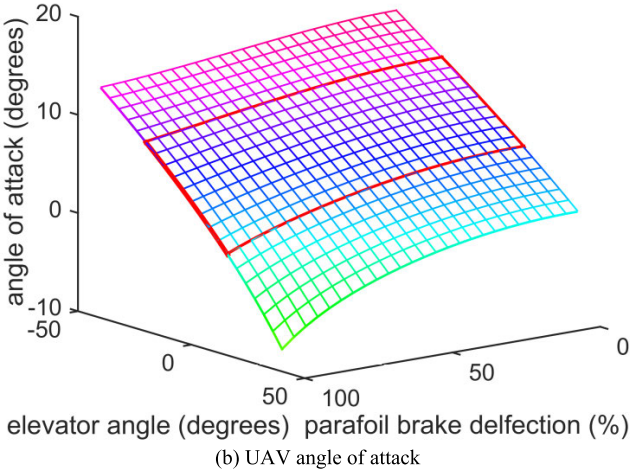

(b) UAV angle of attack

FIGURE 10. Angle of attack under varying parafoil brake defections and UAV elevator control.

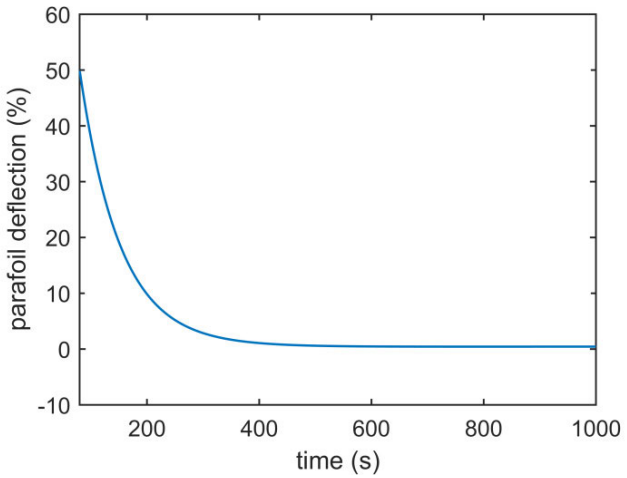

(a) Parafoil brake deflection

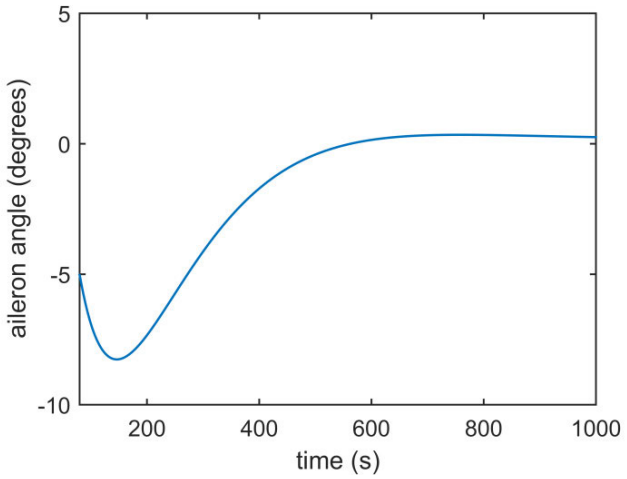

(b) UAV aileron deflection

FIGURE 11. Estimated control input (Case 1).

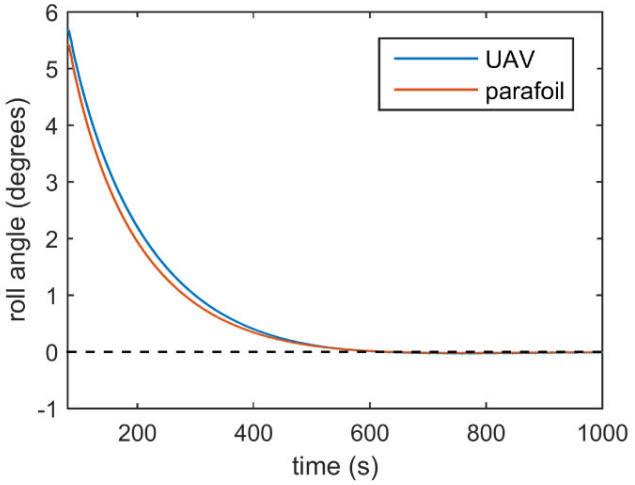

FIGURE 12. Roll angles of the parafoil and the UAV (Case 1).

mechanisms simultaneously and produce the desired attitude of the parafoil-UAV system.

To further illustrate the control performance of the proposed method, comparisons between the multivariate ES-NM controller and the proportional-integral-derivative (PID) controller for Case 2 are provided. In Case 2, there is a unique wind field along the Y_g axis of the inertial reference frame. The wind direction is constant, and the wind speed is variable, as shown in Fig. 13. This situation will cause the parafoil-UAV system to begin a pendulum-swinging motion and increase the risk associated with landing if there is no control. Hence, the control object of these two controllers for Case 2 is to maintain the roll angle of the UAV as close to zero as possible.

The two control mechanisms of the parafoil-UAV system have different control characteristics and applications. For the attitude control of the UAV, the UAV control mechanism plays a dominant role. The parameters of the multivariate ES-NM controller need to be changed. For Case 2, the gain matrix k of the multivariate ES-NM controller is modified to $diag\{10000,\ 100\}$, and the other parameters remain the same. For the PID controller, the aileron deflection is chosen as the input of the control system. The control range is -28 to 28 degrees. k_P, k_I and k_D are tuned as 0.5, 1.05 and 2.1. The simulation results of the PID controller and

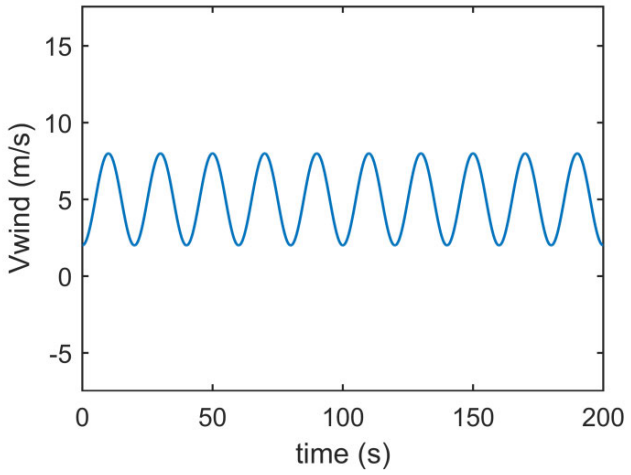

FIGURE 13. Velocity of the wind (Case 2).

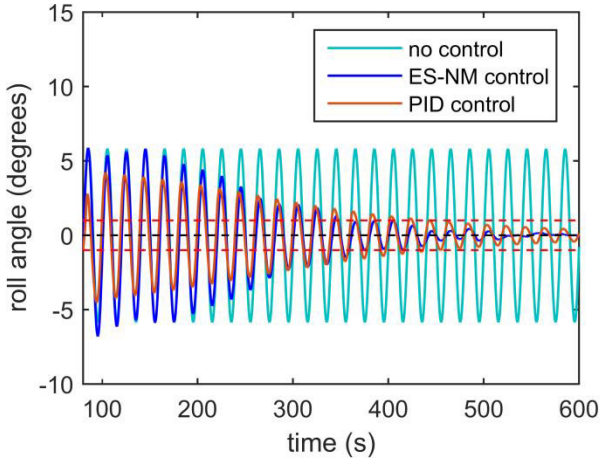

FIGURE 14. Comparison of the UAV roll angles (Case 2).

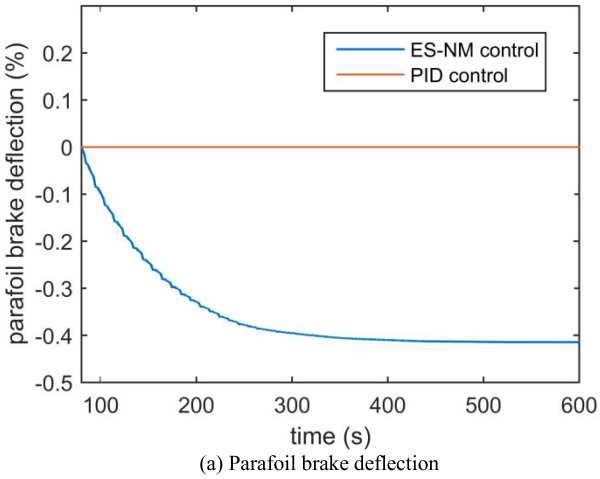

(a) Parafoil brake deflection

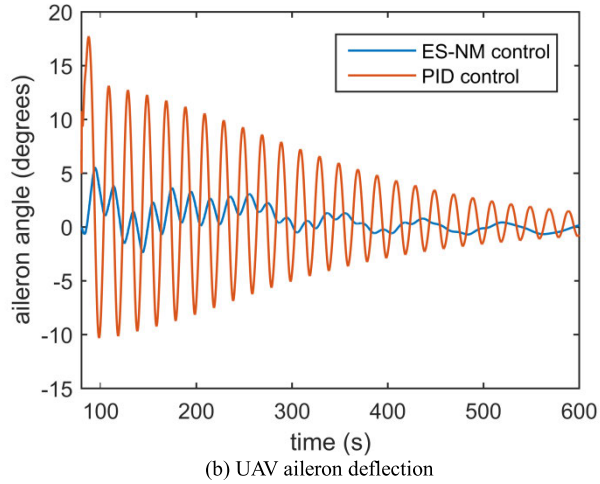

(b) UAV aileron deflection

FIGURE 15. Comparisons of the control inputs (Case 2).

the multivariate ES-NM controller for Case 2 are presented in Figs. 14-15.

As shown in Fig. 14, under the influence of the PID controller and the multivariate ES-NM controller, the roll angles of the UAV both show damped oscillations. The amplitudes of oscillations gradually decrease, and the values converge to zero. At 600 s, the UAV roll angle under the multivariate ES-NM controller is close to zero, and the roll angle under the PID controller is still oscillating. It shows that the response rate of the multivariate ES-NM controller is better than that of the PID controller.

Fig. 15 shows the parafoil brake deflection and the UAV aileron deflection achieved by the PID controller and the multivariate ES-NM controller. For the PID controller, the simulated parafoil brake deflection is zero, and the variation of the UAV aileron is a damped oscillation. The maximum value of the UAV aileron deflection at the beginning can be up to 17.5 degrees. For the multivariate ES-NM controller, parafoil brake deflection exists. Its minimum value is only -0.41%. The UAV aileron deflection is also damped, but the maximum value is less than 6 degrees due to the existence of the parafoil brake deflection. The multivariate ES-NM controller shows a smaller overshoot and is better than the PID controller in terms of energy consumption.

VI. CONCLUSION

In this article, an optimal control method called multivariate ES-NM is introduced to solve the pendulum-swing problem of parafoil-UAV systems. To assess the performance of multivariate ES-NM control, a multibody dynamic model is developed based on the flexible line assumption. Using flight test data, the aerodynamic coefficients are corrected, and the accuracy of the model is verified.

Simulations of this model under varying parafoil brake deflections and UAV control inputs are performed. The results show that the UAV control input permitted by the parafoil-UAV system changes with the increase of the parafoil brake deflection. The coupling effect of these two control mechanisms leads to a decrease in the control range. According to the redesigned control range, the parameters of the multivariate ES-NM controller are confirmed. Simulation experiments are performed under wind and no-wind conditions. As shown in the results, the multivariate ES-NM

control can adjust the parafoil brake deflection and the UAV control input simultaneously and control the attitude angles of the parafoil-UAV system. This proposed control method can effectively solve the pendulum-swing problem. Furthermore, comparisons between the PID controller and the multivariate ES-NM controller are presented. The response rate of the proposed controller is better, and the overshoot is smaller. The performance of the multivariate ES-NM controller is better than that of the PID controller in terms of the energy consumption.

REFERENCES

[1] T. Wyllie, "Parachute recovery for UAV systems," *Aircr. Eng. Aerosp. Technol.*, vol. 73, no. 6, pp. 542–551, Dec. 2001.

[2] T. Wyllie, P. Downs, T. Wyllie, and P. Downs, "Precision parafoil recovery—Providing flexibility for battlefield UAV systems?" in *Proc. 14th Aerodynamic Decelerator Syst. Technol. Conf.*, San Francisco, CA, USA, Aug. 2012, p. 1497.

[3] R. A. Machin, C. S. Iacomini, C. J. Cerimele, and J. M. Stein, "Flight testing the parachute system for the space station crew return vehicle," *J. Aircr.*, vol. 38, no. 5, pp. 786–799, Sep. 2001.

[4] P. Shao, C. Wu, and S. Ma, "Research on key problems in assigned-point recovery of UAV using parachute," in *Proc. IEEE Int. Conf. IEEE Region (TENCON)*, Xi'an, China, Oct. 2013, pp. 1–4.

[5] S. Luo, P. Tan, Q. Sun, W. Wu, H. Luo, and Z. Chen, "In-flight wind identification and soft landing control for autonomous unmanned powered parafoils," *Int. J. Syst. Sci.*, vol. 49, no. 5, pp. 929–946, Feb. 2018.

[6] S. Luo, Q. Sun, P. Tan, M. Sun, Z. Chen, and Y. He, "Soft landing control of unmanned powered parafoils in unknown wind environments," *Proc IMechE G, J. Aerosp. Eng.*, vol. 233, no. 3, pp. 949–968, Jan. 2018.

[7] K. Wise, "Dynamics of a UAV with parafoil under powered flight," in *Proc. AIAA Guid., Navigat., Control Conf. Exhibit*, Summit County, CO, USA, Jun. 2012, p. 6795.

[8] C. Redelinghuys, "A flight simulation algorithm for a parafoil suspending an air vehicle," *J. Guid., Control, Dyn.*, vol. 30, no. 3, pp. 791–803, May 2007.

[9] M. Li, J. Yan, and Y. Liu, "Improved digital model of parafoil-unmanned aerial vehicle accurate recycling system," in *Proc. IEEE Chin. Guid., Navigat. Control Conf. (CGNCC)*, Nanjing, China, Aug. 2016, pp. 1857–1863.

[10] F. Lv, W. He, and L. Zhao, "An improved nonlinear multibody dynamic model for a parafoil-UAV system," *IEEE Access*, vol. 7, pp. 139994–140009, 2019.

[11] K. B. Ariyur, and M. Krstić, *Real-Time Optimization by Extremum-Seeking Control*. Hobokren, NJ, USA: Wiley, 2003.

[12] H. Malek, S. Dadras, and Y. Chen, "Performance analysis of fractional order extremum seeking control," *ISA Trans.*, vol. 63, pp. 281–287, Jul. 2016.

[13] E. Dincmen, B. A. Guvenc, and T. Acarman, "Extremum-seeking control of ABS braking in road vehicles with lateral force improvement," *IEEE Trans. Control Syst. Technol.*, vol. 22, no. 1, pp. 230–237, Jan. 2014.

[14] C. Yin, B. Stark, Y. Chen, S.-M. Zhong, and E. Lau, "Fractional-order adaptive minimum energy cognitive lighting control strategy for the hybrid lighting system," *Energy Buildings*, vol. 87, pp. 176–184, Jan. 2015.

[15] H.-H. Wang, S. Yeung, and M. Krstic, "Experimental application of extremum seeking on an axial-flow compressor," *IEEE Trans. Control Syst. Technol.*, vol. 8, no. 2, pp. 300–309, Mar. 2000.

[16] C. Yin, S. Wu, S. Zhou, J. Cao, X. Huang, and Y. Cheng, "Design and stability analysis of multivariate extremum seeking with newton method," *J. Franklin Inst.*, vol. 355, no. 4, pp. 1559–1578, Mar. 2018.

[17] C. Yin, S. Dadras, X. Huang, J. Mei, H. Malek, and Y. Cheng, "Energy-saving control strategy for lighting system based on multivariate extremum seeking with newton algorithm," *Energy Convers. Manage.*, vol. 142, pp. 504–522, Jun. 2017.

[18] J. Tao, Q. Sun, H. Sun, Z. Chen, M. Dehmer, and M. Sun, "Dynamic modeling and trajectory tracking control of parafoil system in wind environments," *IEEE/ASME Trans. Mechatronics*, vol. 22, no. 6, pp. 2736–2745, Dec. 2017.

[19] S. Müller, O. Wagner, and G. Sachs, "A high-fidelity nonlinear multibody simulation model for parafoil systems," in *Proc. 17th AIAA Aerodynamic Decelerator Syst. Technol. Conf. Seminar*, Monterey, CA, USA, Nov. 2012, p. 2120.

[20] N. Slegers and M. Costello, "Aspects of control for a parafoil and payload system," *J. Guid., Control, Dyn.*, vol. 26, no. 6, pp. 898–905, Nov./Dec. 2003.

[21] O. A. Yakimenko, *Precision Aerial Delivery Systems: Modeling, Dynamics, and Control*. Reston, VA, USA: AIAA, 2015, pp. 282–287.

[22] P. Lissaman and G. Brown, "Apparent mass effects on parafoil dynamics," in *Proc. Aerosp. Des. Conf.*, Irvine, CA, USA, Aug. 2012, p. 1236.

[23] T. M. Barrows, "Apparent mass of parafoils with spanwise camber," *J. Aircr.*, vol. 39, no. 3, pp. 445–451, May/Jun. 2002.

[24] B. L. Stevens, F. L. Lewis, and E. N. Johnson, *Aircraft Control and Simulation*, 3rd ed. Hobokren, NJ, USA: Wiley, 2016, pp. 108–115.

[25] D. Jung and P. Tsiotras, "Modeling and Hardware-in-the-Loop simulation for a small unmanned aerial vehicle," in *Proc. AIAA Infotech Aerospace Conf. Exhibit*, Rohnert Park, CAA, USA, Jun. 2012, p. 2768.

[26] C. Montalvo and M. Costello, "Avoiding lockout instability for towed parafoil systems," *J. Guid., Control, Dyn.*, vol. 39, no. 5, pp. 985–995, May 2016.

[27] J. Kyle and M. Costello, "Comparison of measured and simulated motion of a scaled dragline excavation system," *Math. Comput. Model.*, vol. 44, nos. 9–10, pp. 816–833, Nov. 2006.

[28] A. Ghaffari, M. Krstić, and D. Nešić, "Multivariable newton-based extremum seeking," *Automatica*, vol. 48, no. 8, pp. 1759–1767, Aug. 2012.

[29] W. Wu, Q. Sun, M. Sun, M. Dehmer, and Z. Chen, "Modeling and control of parafoils based on computational fluid dynamics," *Appl. Math. Model.*, vol. 70, pp. 378–401, Jun. 2019.

[30] M. Ghoreyshi, K. Bergeron, A. J. Lofthouse, and R. M. Cummings, "CFD calculation of stability and control derivatives for ram-air parachutes," in *Proc. AIAA Atmos. Flight Mech. Conf.*, San Diego, CA, USA, Jan. 2016, p. 1536.

[31] C. Ye and D. Ma, "Aircraft dynamic derivatives calculation using CFD techniques," *J. Beijing Univ. Aeronaut. Astronaut.*, vol. 39, no. 2, pp. 196–200, Feb. 2013.

FEIKAI LV received the B.S. degree in aircraft design and engineering from Northwestern Polytechnical University, Xi'an, in 2010, and the M.S. degree in spacecraft engineering from Beihang University, Beijing, in 2014, where he is currently pursuing the Ph.D. degree in spacecraft engineering with the School of Astronautics.

His research interests include modeling and simulation, as well as flight dynamic and robust control for parafoil systems.

WEILIANG HE received the B.S. degree in aircraft design from the Nanjing University of Aeronautics and Astronautics, Nanjing, China, in 1987, the M.S. degree in spacecraft engineering from the China Academy of Space Technology, Beijing, in 1990, and the Ph.D. degree in spacecraft engineering from Beihang University, Beijing, China, in 2006.

His research interests include spacecraft system design, spacecraft reentry and landing technology, and inflatable space structure system.

LINGGONG ZHAO received the B.S. degree in applied physics from Shandong University, Ji'nan, China, in 2011. He is currently pursuing the Ph.D. degree in aeronautical and astronautical science and technology with the School of Astronautics, Beihang University. His research interests include flight dynamic and unmanned aerial vehicle control.